Femtosecond photodissociation dynamics by velocity map imaging. The methyl iodide case

Rebeca de Nalda[1], Luis Rubio-Lago[2], Vicent Loriot[1,2] and Luis Bañares[2]

[1] Instituto de Química Física Rocasolano, CSIC, C/ Serrano, 116, 28004 Madrid, Spain.
[2] Departamento de Química Física, Facultad de Ciencias Químicas, Universidad Complutense de Madrid, 28040 Madrid, Spain.

ABSTRACT

The introduction of time-resolved measurements in the femtosecond time-scale using velocity map imaging techniques of charged particles (ions and photoelectrons) in combination with resonant multiphoton ionization of the fragments for the study of the photodissociation dynamics of small polyatomic molecules is reviewed. A typical experiment consists on the measurement of a sequence of images, whose analysis requires in most cases sophisticated multidimensional fitting methods to extract all the relevant time-resolved information contained in the images. In particular, the application of these techniques to the study of the direct photodissociation (*A* band) and electronic predissociation (*B* band) of methyl iodide along with the detection and characterization of transient species and the study of cluster dissociation, as a case example for femtosecond velocity map imaging, are presented and discussed.

1. INTRODUCTION

In the last decades, the field of laser photochemistry has reached an important technical maturity, due to the development of versatile laser sources and powerful detection techniques. One of the followed directions has aimed to explore dynamics directly in the time scales of chemical molecular processes, which are typically in the femtosecond to picosecond range. Understanding the time required for a process to take place - if such concept is suitable of a precise definition within the realm of the microscopic world - implies the possibility of either measuring, or externally inducing, the start and finish moments of the process. In standard two-body reaction dynamics, the definition of the start of the reaction is arbitrary, given the long-range potentials involved in a chemical reaction, and this is complicated by the fact that in conventional experiments, performed with a large number of molecules, each event is characterized by its own impact parameter, relative velocities and positions, so that, for the ensemble, the origin of time is particularly ill-defined in the scale characteristic of the reaction itself.

On the contrary, photo-induced processes (photoionization, photoisomerization, photodissociation) are often termed "half reactions" [1], with an origin of time that is set by the laser pulse initiating the process. Some degree of uncertainty remains, however, due to the temporal width of the laser pulse, and thus time zero is best defined for the shortest pulse available. In practice, it is common to assign the origin of time to the maximum of the intensity envelope of the laser pulse used to induce a given process. It is the temporal width of the laser pulse that sets the time resolution and hence, the time scales that can be explored with such pulse. Even for half reactions, however, the end of the process remains considerably less well defined, and in practice, the most useful definition depends on the technique to be used as a probe of the process. If a short non-resonant laser pulse is employed as an ionization probe, transition state species can be subjected to ionization at all times, and one would have to define the "end" of the process as the time delay for which some parameter characteristic of the process (i.e. the kinetic energy distribution) reaches its asymptotic value. The situation is different if a short laser pulse, resonant with an intermediate level of a product fragment, is employed as probe in a stepwise ionization process (REMPI), or in a transition to a fluorescence emitting state. The presence of the resonance enhances the magnitude of the observable, be it fluorescence or ionization, by orders of magnitude with respect to the non-resonant case. In this instance, only if the co-fragment is distant enough, so that the targeted resonance is not shifted beyond the bandwidth of the probe laser, is the product fragment detected with high efficiency. Typically, the probe laser central wavelength is tuned to the free radical resonance, so that detection only starts when the fragments are far from each other so that the above condition is fulfilled. This is normally referred to as "the opening of the optical window". This type of measurement provides a natural definition of the "end" of the process, allowing "clocking", although it has to be noted that it is a definition that is dependent on the bandwidth of the probe laser [2]. In any case, comparison of "clocking" times in multichannel processes allows to extract information on the energy flow processes between electronic and nuclear degrees of freedom in a molecular species, and can provide valuable information on the dynamics at special regions of the potential energy surfaces like conical intersections.

The study of these fast energy distribution processes in molecules has been at the core of the discipline that has been termed Femtochemistry for the last decades [3]. In the heart of the gear of such progress, several molecular systems, which possess the valuable characteristic of being complex and yet theoretically accessible, can be found. Among

them, methyl iodide, CH_3I, constitutes the five-atom paradigm [4]. Due to the high electronegativity of the halogen atom, methyl halides can be viewed as pseudo-diatomic systems (where the methyl moiety plays the role of a pseudo-atom), pseudo-triatomic (the pseudo-atom consists of the three hydrogen atoms) or full five-atom molecules, depending on the theoretical framework. What makes methyl iodide more amenable to experimentalists with respect to other methyl halides, however, is related to the strong spin-orbit splitting of the iodine atom, which has several consequences. In the first place, the CH_3I absorption spectrum is notably shifted towards the red with respect to the other methyl halides. The first absorption band in methyl iodide, the *A* band, is centered at 262 nm; in methyl bromide and methyl chloride, it lies at around 200 nm and 170 nm, respectively. The difference is meaningful, since the absorption spectrum in methyl iodide can be explored in detail due to the availability of tunable laser sources, while in the other two cases, only discrete studies at particular wavelengths are feasible. In the second place, despite the structureless shape of the methyl iodide *A* band, quasi-selective excitation of any of the three bright states is possible, while in the other methyl halides, the three states are highly overlapped across the spectral range. Spectroscopic convenience is also related to the existence of a variety of readily accessible (2+1) REMPI schemes for all possible products of the reaction, the methyl radical $CH_3(\tilde{X}\,^2A_2)$, the ground state iodine atom $I(^2P_{3/2})$ and the spin-orbit excited $I^*(^2P_{1/2})$. The second absorption band of CH_3I, also named *B* band, possesses a completely different character, and consists of transitions to lifetime broadened bound states of Rydberg character. It is an interesting example of predissociation where lifetimes critically depend on the details of the coupling to the dissociative continuum. The importance of methyl iodide in the field of photodissociation dynamics cannot be reduced to a role of testing bench. The CH_3I photodissociation process possesses its own dynamical interest, which can be explained in terms of molecular structure considerations. The C_{3v} symmetry of methyl iodide can be easily lowered to C_s with low-energy vibrations. Such change in geometry dictates the whole photochemistry both in the *A* and *B* band, enabling curve crossings that would not be possible in C_{3v}.

In the chapter, we will describe recent results of the prompt (≈100 fs) CH_3I and $(CH_3I)_2$ dissociation in the *A* band and the slower predissociation (≈1 ps) in the *B* band, studied through the combination of ultrashort tunable pump-probe laser schemes with detection of velocity map ion and electron images (see Figure 1 for a view of the relevant potential energy curves). Attention will be paid to some crucial issues that are sometimes overlooked, like the applicability of REMPI schemes in ultrafast experiments, the role of laser-induced molecular alignment, or the influence of the optical coupling window on reaction “clocking” times. Additionally, we will show how these processes can be dramatically altered by the presence of a nearby molecule. The CH_3I molecule possesses a significant permanent dipole moment and readily forms clusters for sufficiently high densities and low temperatures. This chapter will show the dramatic effects of dimerization on the dissociation dynamics.

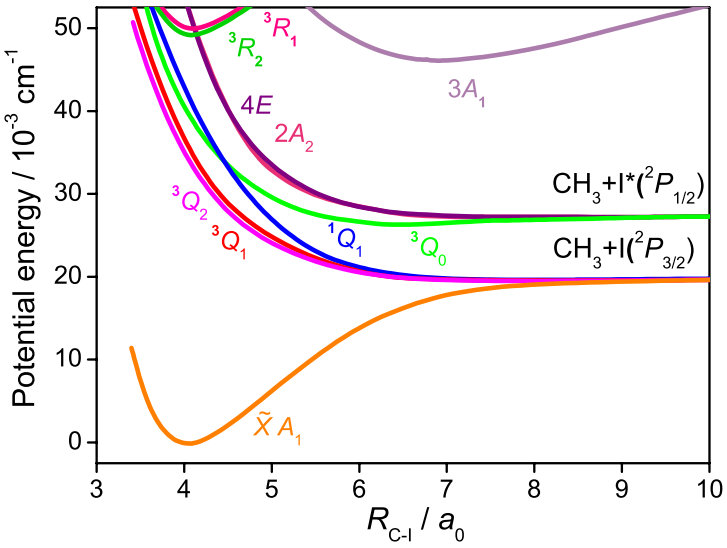

Figure 1. Relevant potential energy curves for CH_3I photodissociation and electronic predissociation calculated along the reaction coordinate (C-I distance). Adapted from A. B. Alekseyev et al., J. Chem. Phys., 134, 044303 (2011).

2. METHODOLOGY

2.1. The experiment: Femtosecond velocity map imaging

One of the central ingredients of the experimental strategy employed here is the use of the velocity map imaging technique, presented for the first time by Eppink and Parker in 1997 [5]. This technique permits full three-dimensional (3D) spatial resolution of the velocity distribution of charged particles, which, coupled to femtosecond pump-probe detection, leads to a complete real time elucidation of the dissociation event. Figure 2 shows a typical sketch of the experimental setup.

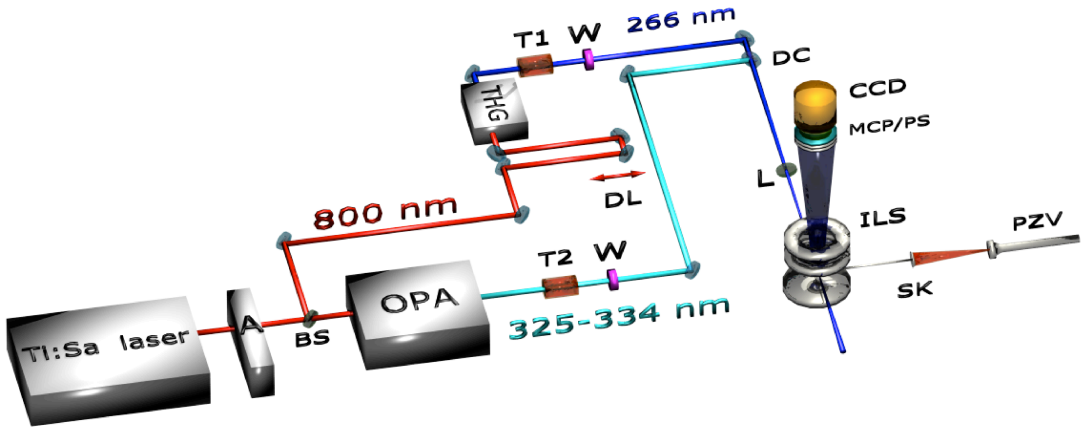

Figure 2. Schematic representation of the setup for femtosecond time-resolved velocity map imaging experiments. A Ti:sapphire amplified laser system is split into two arms that provide the frequency-tripled pump beam (266 nm) and the tunable probe beam [325-334 nm, output of an optical parametric amplifier (OPA)]. (BS) Beam splitter. (A) Autocorrelator. (W) Half-wave plate. (T1,T2) Telescopes. (L) Lens. (DC) Dichroic mirror. (DL) Delay line. (PZV) 1 kHz piezoelectric valve. (SK) Skimmer. (ILS) Ion lens system. (MCP) Microchannel plate. (PS) Phosphor screen. (CCD) Charge-coupled device camera. Copropagating pump and probe femtosecond pulses are focused in the CH3I/He molecular beam. The 3D distribution of a given fragment ion is extracted, accelerated, and projected on an imaging detector consisting of a MCP/PS coupled to a CCD camera, where the velocity map images are recorded as a function of pump-probe delay time.

The irradiation configuration and pulse parameters (central wavelengths and energies) are chosen as a function of the experiment performed as variants of a single main rig. For most of the experiments described here the laser was a Spectra-Physics amplified Ti:sapphire system delivering 80 fs, 1 mJ pulses centered at 800 nm with 1 kHz repetition rate, but some of the later experiments (*B*-band) were performed with an upgraded system (50 fs, 3.5 mJ). For two-pulse experiments, the fundamental output is split into two arms, one of which is used to pump an optical parametric amplifier (OPA) tuned to generate signal pulses in the 1.2 μm–1.4 μm region, which are later frequency quadrupled to constitute a ~3 μJ beam in the 300-340 nm region for (2+1) REMPI probing of either I atoms or CH_3 fragments. In the non-resonant experiments, the OPA is not used and the ~800 nm beam constitutes the probe beam, which is later recombined with the pump beam. The pump beam is generated by harmonic generation (third harmonic for the *A*-band, fourth for the *B*-band) of the second arm of the fundamental output, yielding 266 nm or 200 nm, respectively. A computer-controlled, motorized delay stage in the pump arm provides controllable delay between the pump and probe pulses with around 0.3 fs precision.

For *A*-band studies in CH_3I, performed with a third-harmonic pump pulse, the time duration of the pump and probe pulses is estimated to be around 100 fs, limited by a ~200 fs cross correlation. Later *B*-band studies, pumped with the fourth harmonic at 200 nm, showed a ~400 fs cross correlation. The bandwidth of both pump and probe lasers is ~3 nm full width at half maximum (FWHM), except the 200 nm beam used for *B*-band studies, with a bandwidth of only ~0.3 nm FWHM. Independent polarization control in each arm is provided by the use of half-wave plates, and telescopes are used to control their focusing geometry on target. The pump and probe laser beams are propagated into the vacuum chamber collinearly and focused with a 25 cm focal length lens into the interaction region of the chamber. Their polarization is kept parallel to the detector face to provide the cylindrical symmetry required for the procedure of Abel inversion of the ion images.

The vacuum chamber is divided into three sections: source, ionization, and detection, with differential pumping between the source chamber and the other two. The molecular beam is generated by supersonic expansion of the sample. CH_3I, kept at a temperature of 0 °C or below in ice/water or ice/salt baths, is seeded in Ar or He, at a typical total pressure of 1.5–2.5 bars, depending on signal levels, and expanded into vacuum through the 0.5 mm nozzle diameter of a 1 kHz piezoelectric home-made pulsed valve. The choice of temperature, buffer gas pressure and temporal section of the gas pulse allows control of the degree of clustering. Experiments devoted to CH_3I monomer dissociation were conducted under conditions where no clustering occurred. The molecular beam passes through a 0.5 mm skimmer that separates the source chamber from the ionization chamber. Once in the ionization chamber the molecular beam flies between the repeller and the extractor plates of a gridless ion lens electrode system, where is intersected perpendicularly by the laser beams. The ions created in the interaction region are extracted perpendicularly towards a 60 cm time-of-flight tube at the end of which sits the detector, a dual microchannel plate (MCP) in Chevron configuration coupled to a phosphor screen. Appropriate voltages to the electrodes are applied so that velocity mapping configuration [5] is achieved, *i.e.*, all ions with the same initial velocity vector are mapped on the same point on the plane of the detector, regardless of their original position. Optimum velocity mapping conditions were obtained with $V_{extractor}$ /$V_{repeller}$=0.785 at $V_{repeller}$=5200 V. By applying a gated voltage to the front plate of the MCP, its gain is gated, so that a selective detection of ion masses can be achieved. The two-dimensional (2D) mass-selected ion images on the phosphor screen are recorded with a Peltier-cooled 12-bit CCD camera and stored in a computer. The velocity, and thus the kinetic energy, of the

ions, was calibrated using methyl images produced in the *A*-band photodissociation of CH_3I for a long time delay between the pump and probe pulses, using the known kinetic energy release of the $CH_3(\nu=0)+I^*(^2P_{1/2})$ and $CH_3(\nu=0)+I(^2P_{3/2})$ channels [4]. In these conditions, the kinetic energy resolution of the apparatus is better than 100 meV at 1 eV kinetic energy release.

Raw images are projections of the Newton spheres characteristic of the photodissociation process on the plane of the detector. They can be Abel-inverted [6] in the case of cylindrical symmetry, which is guaranteed if the polarization axes of all lasers employed are parallel to the plane of the detector. The method used for inversion was pBasex [7], where polar coordinates are applied for the inversion. This way, the noise produced in the mathematical procedure is concentrated in the middle of the image, allowing a clean analysis of the images in the regions of interest.

Time zero, defined as the position of temporal overlap between the pump and probe lasers on target, and also their cross-correlation function, are given by the *in situ* measurement of either the parent ion transient of *N*,*N*-diethyl aniline by (1+1') REMPI [4] or through multiphoton ionization of Xe [8].

The energy balance for the photodissociation of CH_3I is given by

$$E_T = \frac{m_I}{m_{CH_3I}}\left[h\nu - D_0 + E_i(CH_3I) - E_{SO}[I(^2P_{j/2})]\right] \quad (1)$$

where E_T is the center-of-mass translational energy of the $CH_3(\nu)$ fragment, ν is the frequency of the photolysis laser, D_0 =2.41 ± 0.03 eV [9] is the dissociation energy of the C–I bond, $E_{SO}[I(^2P_{j/2})]$ is the spin-orbit energy for the iodine atom in the ^2P state (for I, E_{SO}=0 and for I*, E_{SO}=0.943 eV) [9] and $E_i(CH_3I)$ is the internal energy (rotation and vibration) of the parent molecule in the molecular beam. For a given photolysis wavelength, the available energy for the methyl moiety is

$$E_{av} = h\nu - D_0 - E_{SO}[I(^2P_{j/2})] = E_T + E_i(CH_3I) \quad (2)$$

The angular distributions for each fragment channel, obtained by radial integration of the corresponding images, have been fitted to the commonly used expression for one-photon dissociation and (2+1) REMPI detection processes:[10]

$$I(\theta) = \frac{\sigma}{4\pi}\left[1 + \beta_2 P_2(\cos\theta) + \beta_4 P_4(\cos\theta) + \beta_6 P_6(\cos\theta)\right] \quad (3)$$

where θ is the angle between the photofragment recoil direction and the photolysis laser polarization direction, σ is the absorption cross section (since the experimental setup has been not calibrated for total intensities, σ is treated as a normalization fitting parameter), β_i are anisotropy parameters which reflect the dissociation dynamics and the photofragment polarization, and P_i are the Legendre polynomials of i^{th} order. If no photofragment polarization is expected, Eqn. (3) can be truncated in i=2, and in that particular case, β_2 coincides with the anisotropy parameter, β.

2.2. The multidimensional analysis

This section is devoted to details concerning image analysis for the particular case of velocity map charged particle images. It is common that the analysis of such data is carried out using methods that involve cuts or partial integrations through the multidimensional data. As a consequence, in many instances, the full information that can be extracted from the data is not totally and accurately recovered. A homemade procedure developed in our group [8] for the complete multidimensional fit of this type of data will be described here. This procedure has proven to be crucial for the extraction of all the relevant information from the images if, in addition, the temporal dimension is included, as it is the case in time-resolved velocity map imaging experiments. Some examples can be seen in [11,12]. The key advantage of the method consists of its capability to distinguish the different overlapped contributions present in the set of images corresponding to different reaction channels of interest from secondary signals arising from other pathways.

Briefly, the method consists of an application of the well-known Levenberg–Marquardt nonlinear regression method [13] to *n*-dimensional data, but adapted to the particular case of velocity map images to find a balance between calculation speed, accuracy, and human-guided input. The procedure assumes that each image contains the sum of a number of “contributions” (related to each of the mechanisms producing a given species with a certain speed distribution). Each contribution is parameterized as a function of all variables (radius and angle for each image, but also time, for instance, to fit a time-dependent series of images) with a test functional form with physical meaning using a sufficient number of adjustable parameters. The first test functions are chosen guided by the known physical properties of the system. The least-squares procedure is then applied to the complete data collection. Inspection of the residuals (typically, also in image format), guides the choice of the second set of functional forms. An iterative procedure of this kind allows the complete parameterization of the data, and from this, quantities such as decay times, anisotropy parameters, etc. can be obtained for each contribution, with estimates of error bars. For those cases where the initial guesses for the parameters or functional forms are misguided (on the number or nature of the contributions to the image, on the time behavior of anisotropy, etc.), discrepancies can be detected easily through the use of the analysis of the residuals. It is important to note that the multidimensional nature of the fit allows the discrimination of the different contributions to the images, in a manner that a reduced-dimensionality analysis cannot achieve. In addition, there is no conceptual problem to extend the fitting procedure to *n* dimensions, the only limitation being computational time restrictions to analyze large quantities of data. Once the procedure has yielded an analytical expression for the complete set of data, the behavior of each "contribution" can be analyzed separately.

A typical image acquired in this type of experiments, either raw (through slice imaging), or, equivalently, mathematically inverted (through velocity-map imaging), contains, in general, a set of ”contributions”, by which we mean each of the possible processes or channels associated with a given type of charged particle (ion or photoelectron). Typically, a ”channel” is characterized by a given kinetic energy, which, on the image, can be measured by the distance to the center of the image, *r*. For the analysis of the kinetic energy distribution (ignoring the angular character), integration over the 2π angular range of the images is carried out. The signal $S(v,t)$, depending on speed (v) and time (t), is assumed to be composed of individual contributions $C_i(v,t)$, each of which has its own temporal shape as a function of time, $i(t)$, and speed distribution, $R_i(v)$. However, $C_i(v,t)$ does not need to be separable, in the sense that some of the parameters of $R_i(v)$ may be allowed to depend on time. It is assumed, in general, that these contributions do not

interfere with each other, so that $S(v,t)=\Sigma_i C_i(v,t)$. Such contributions can be modeled, for instance, by asymmetric-Gaussian functions such as

$$R(v) = e^{-4\ln 2[(v-v_0)/\sigma_r]^2} H(v-v_0) + e^{-4\ln 2[(v-v_0)\sigma_l]^2} H(v_0-v) \quad (4)$$

where v_0 is the position of the peak, σ_r and σ_l are the right and left widths, respectively, and $H(v)$ is the Heaviside function. The physical meaning of the asymmetry in the peaks of the speed distribution is related in most cases to the rotational temperatures of both the parent molecule and the nascent fragment, convoluted by the apparatus response function. The temporal behavior can show different functional forms depending on the type of mechanism. For the non-resonant multiphoton ionization detection, it defines a cross-correlation-type signal. For the cases where no changes in the shape of each contribution are expected as a function of time, we can write

$$C_i(v,t) = i(t) \times R_i(v). \quad (5)$$

The angular distribution of charged particles for a given radius provides additional information on the nature of the channel. For the type of analysis that we are describing, it simply adds another layer of complexity. Legendre polynomials, $P_n(\cos\alpha)$, represent a complete angular basis set, which has the advantage that only few terms β_n are generally sufficient to describe the anisotropy of each contribution. The anisotropy A can be written as

$$A(\alpha) = 1 + \beta_2 P_2(\cos\alpha) + \beta_4 P_4(\cos\alpha) + \cdots \quad (6)$$

where α is the angle between the polarization axis of the electric field and the considered direction.

In practice, a strategy that has proven most useful as a pre-treatment of the experimental data is to perform partial angular integration of the set of images in 10° steps. This way, for the 90° quadrant relevant if cylindrical symmetry holds, nine speed distributions are extracted from each image corresponding to the different angular ranges. These are stored in a 3D matrix with the dimensions speed, angular section, and time.

For best results, it is common that a global fit to all experiments performed in identical conditions is carried out. In that case, each experiment is labeled in order, and the label is taken as an additional "dimension" for the fit. Such strategy takes into account that some of the parameters (relative intensity of the multiphoton processes, time of temporal overlap, etc.) may have differing values among experimental runs, but some others (decay times, for instance) must all share a given value.

Finally, the Levenberg–Marquardt nonlinear regression method is applied to fit the parameters in the "constructed" images for least discrepancy with the experimental set of data. This methodology has proven extremely efficient for the extraction of meaningful values for physical parameters (temperatures, anisotropy parameters, population level distributions, lifetimes, cross-correlations) from the complex data provided by extended sets of images acquired in experiments.

3. THE *A* BAND

The decomposition dynamics of CH_3I upon UV photon absorption in the *A* band constitutes one of the most extensively documented cases of the consequences of non-adiabatic surface-crossing in molecular dynamics. Electronic non-adiabatic interactions, which involve the breakdown of the Born–Oppenheimer approximation, are ubiquitous and considerable theoretical and experimental efforts have been made to characterize the broad variety of possibilities. In particular, conical intersections in polyatomic molecules attract special interest [14,15], partly because they have been identified as candidates for control under strong laser fields [16]. The effect of a conical intersection can be quite complex since it does not need to be energetically accessible to affect the molecular dynamics [17]. When the conical intersection lies close to the Franck–Condon region, as in the case of the alkyl halides in general and in CH_3I in particular, [18] the strong interaction between the involved states plays a major role on the dissociation dynamics.

The CH_3I *A*-band constitutes the lowest-energy absorption feature of the molecule and consists of a broad featureless continuum ranging from 210 to 350 nm with a maximum at about 260 nm [19]. As was first demonstrated by Mulliken and Teller [20], the lowest energy electronic excitation in CH_3I corresponds to an n-σ transition, where a non-bonding *p* electron of iodine is promoted to the lowest energy available anti-bonding molecular orbital [20]. The spin–orbit (SO) coupling is large, due to the presence of the heavy iodine atom, and the SO configuration can be used for the first excited electronic states [21]. Three SO states are accessible through dipole allowed transitions from the ground state: the $^3Q_1$ and $^1Q_1$ states (in Mulliken's notation) [22] through weak perpendicular transitions and the $^3Q_0$ state through a strong parallel transition [23]. The $^3Q_0$ state correlates adiabatically with $CH_3(X^2A_2)$+I*($^2P_{1/2}$) products, while the $^3Q_1$ and $^1Q_1$ states correlate with $CH_3(X\ ^2A_2)$+I($^2P_{3/2}$). From now on we will use I* and I to refer to I*($^2P_{1/2}$) and I($^2P_{3/2}$), respectively, and just CH_3 to refer to $CH_3(X^2A_2)$. At the curve maximum, around 260 nm, the absorption is dominated by the $^3Q_0$ state, while transitions to the $^3Q_1$ and $^1Q_1$ states become more important towards the low energy (red) and high energy (blue) regions of the absorption band, respectively [22,24]. The asymptotic correlation between excited surfaces and photoproducts implies that a curve crossing between the $^3Q_0$ and $^1Q_1$ states must take place close to the Franck–Condon region.

Structurally, the non-adiabatic curve crossing implies a reduction of the molecular symmetry from C_{3v} to C_s caused by *e*-type vibrations during the absorption step [25,26]. In the C_{3v} geometry, the different symmetries of the $^1Q_1$ (3*E*) and $^3Q_0$ ($^2A_1$) states disable any possible crossing. In the reduced symmetry C_s geometry, the 3*E* state splits into 4*A*' and 2*A*'' components, whilst the symmetry of the $2A_1$ state is lowered to 3*A*'. The avoided crossing between the distorted 3*A*' and 4*A*' states gives rise to a conical intersection. The position of the crossing point reported in the literature is strongly dependent on the level attained in the theoretical calculations.

An important feature of CH_3I dissociation in the *A* band, as evidenced experimentally [27], is that approximately 90% of the available energy appears as fragments' kinetic energy, although a substantial vibrational excitation in the umbrella mode (ν_2) of CH_3 has been found. This is expected from the dramatic geometrical change of CH_3 upon dissociation, from pyramidal to planar. Excitation in the CH_3 symmetric stretch mode (ν_1) has been observed too. Methyl fragments in correlation with the ground state I($^2P_{3/2}$) atom appear with a higher internal energy content, both vibrational and rotational than those formed in correlation with spin-orbit excited I($^2P_{1/2}$).

3.1. Reaction clocking: the resonant experiment

This section will describe experiments of the “clocking” type, *i.e.* where the reaction times for the multiple channels are the observables of interest. In the basic experiment, a pump laser is employed to promote the parent molecule to a particular excited state. A second laser, tuned to a resonant transition of a particular photoproduct, is sent to the interaction region after a controllable delay, and ionizes the product fragment of interest. The resonant probe laser opens up an optical coupling region in the potential energy surface determined by the laser bandwidth, which allows the clocking of the reaction from the initial wave packet formed in the Franck–Condon region to the free fragments in the asymptotic region. Since *A*-band photofragmentation happens along purely dissociative surfaces, the dynamics are of “ballistic” nature, and the signal appearance is delayed with respect to the zero of time, at a delay time that we will call the “clocking“ time. The plot of the fragment ion signal intensity versus the delay between the laser pulses can typically be fitted to a Boltzmann sigmoidal curve of the form

$$S \propto \left\{1 + \exp\left(\frac{t - t_0}{t_C}\right)\right\}^{-1} \tag{7}$$

parameterized by a center temporal position t_0 (*i.e.*, delay time for which the intensity has reached half its asymptotic value) and a rise time constant t_C, which describes the steepness of the rise. Relative reaction times of the different channels can be defined through the differences in the center temporal position for their rise curves. Absolute determination of reaction delay times can be determined through an external reference in an independent experiment, and are subject to greater uncertainty.

Upon photodissociation of methyl iodide in the *A* band, the appearance of either atomic iodine or CH_3 fragments can be probed by using their (2+1) REMPI schemes. As a first example, we will show the results of methyl detection when photodissociation is produced at 266 nm. Probe central wavelengths are in the region 320-335 nm and can be tuned to probe the desired components of the nascent CH_3 vibrational wave packet.

Figure 3 shows a series of six Abel-inverted images corresponding to methyl fragments measured for different pump-probe delay times when the probe laser is tuned to 333.5 nm, corresponding to the *Q* branch of the $3p_z(^2A_2'' \leftarrow {}^2A_2'')$ 0_0^0 transition. The first image, acquired at −300 fs, corresponds to the situation where the probe pulse temporally precedes the pump. The unstructured contribution in the center of the image (*i.e.*, low kinetic energy), has been attributed to multiphoton ionization processes. As the pump-probe delay is increased, the appearance of rings indicates the occurrence of reaction channels with a well defined kinetic energy. Since the process is direct and takes place along a purely repulsive surface, the process is fast and can be considered completely terminated (or "asymptotic") after a time delay of approximately 400 fs.

Three rings can be observed in the images. The inner, and most intense ring, and the outer ring correspond to vibrationless $CH_3(\nu=0)$ formed in correlation with I* and I, respectively. It is important to note that a third, weaker ring, can be seen between the two main ones. This can be assigned to CH_3 with one quantum in the ν_1 symmetric stretch mode, in correlation with I, as derived from the measured kinetic energy. $CH_3(\nu_1=1)$ is visible in this experiment, contrarily to nanosecond experiments, because the *Q* branch of the $3p_z(^2A_2'' \leftarrow {}^2A_2'')$ 1_1^1 transition is shifted only by 0.4 nm to the red of the $3p_z(^2A_2'' \leftarrow {}^2A_2'')$

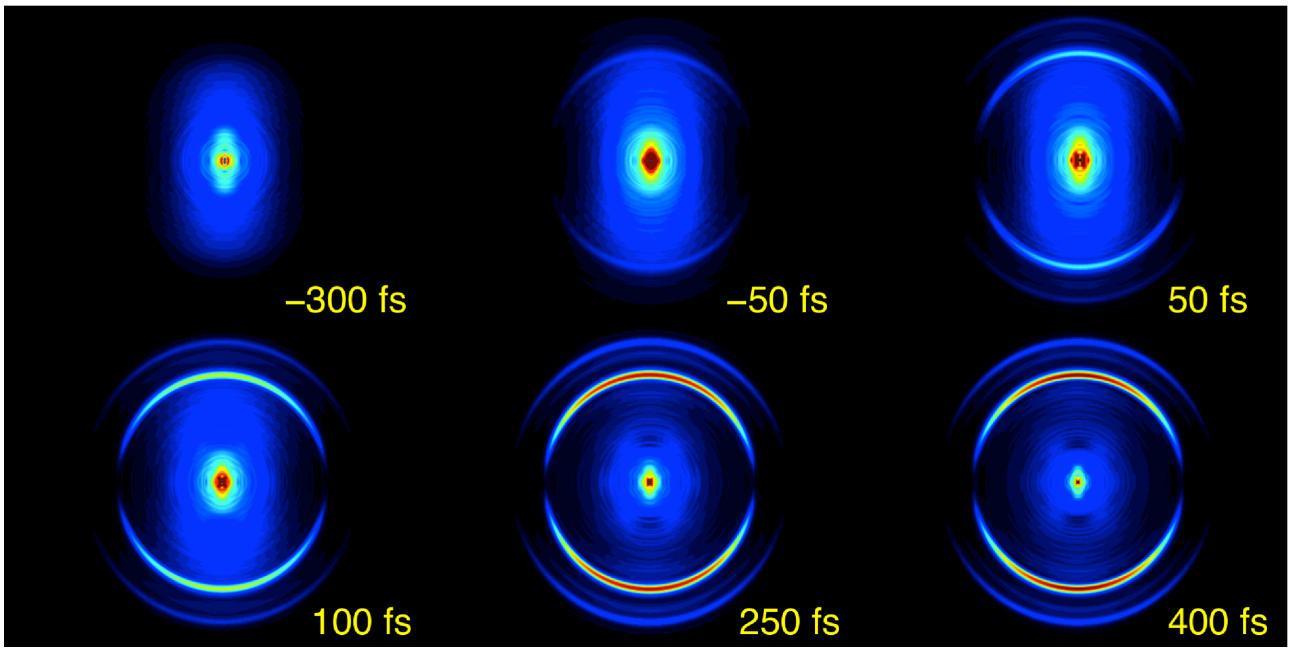

Figure 3. Abel inverted CH_3^+ images obtained upon CH_3I excitation at 266 nm and CH_3 (2+1) REMPI at 333.5 nm - *Q* branch of the $3p_z(^2A_2'' \leftarrow {}^2A_2'')$ 0_0^0 transition- as a function of pump-probe delay time. The central structure is due to multiphoton ionization processes that are produced by each of the laser pulses separately. Three well-defined rings appear in the image for positive delay times. The inner and outer rings correspond to vibrationless $CH_3(\nu=0)$ formed in correlation with spin-orbit excited $I^*(^2P_{1/2})$ and ground-state $I(^2P_{3/2})$ fragments, respectively. The middle ring corresponds to the channel yielding symmetric stretch mode excited $CH_3(\nu_1=1)$ in correlation with the $I(^2P_{3/2})$ fragments.

0_0^0 transition; that is, well within the bandwidth of the femtosecond probe laser centered at 333.5 nm. This phenomenon is quite general when performing REMPI experiments with broadband femtosecond laser pulses, where all transition resonances that lie within the bandwidth of the probe pulse can be strongly enhanced and contribute to the observed signals [4,28].

Angular integration of the images shown in Figure 3 renders the center-of-mass (CM) translational energy distributions of the CH_3 fragment, which are shown in Figure 4. The three peaks in the distribution profile correspond to each of the rings present in the images of Figure 3. The width of the peaks is mainly due to the rotational envelope of the probed rotational distribution, with considerably hotter character for the $CH_3(\nu=0)+I(^2P_{3/2})$ channel than for the $CH_3(\nu=0)+I^*(^2P_{1/2})$ channel, in agreement with previously reported results [29,30]. Additionally, the distributions shown in Figure 4 provide the branching ratio between the I and I* channels (I / I*) in correlation with vibrationless methyl. An asymptotic value of 0.11±0.02 was obtained, in agreement with previous works [31-33].

Radial integration of the images across the radii corresponding to each of the rings yields angular distributions for each channel. For one-photon transitions, and in the absence of fragment alignment, we expect an angular dependence of the form $I(\theta)=(\sigma/4\pi)[1+\beta P_2(\cos\theta)]$, where σ is the total absorption cross section, θ is the angle between the polarization axis of the photolysis laser and the fragment velocity vector, β is the anisotropy parameter, and $P_2(\cos\theta)$ is the second Legendre polynomial. From least-squares fits to this function, asymptotic values (*i.e.*, for a long pump-probe delay time) obtained for the β parameter are 1.89±0.05, 1.69±0.05, and 1.84±0.08 for the $CH_3(\nu=0)+I^*(^2P_{1/2})$, $CH_3(\nu=0)+I(^2P_{3/2})$, and $CH_3(\nu_1=1)+I(^2P_{3/2})$ channels, respectively, in good agreement with previous values reported in the literature. No significant changes in

the anisotropy parameter are observed as a function of time with respect to that of the asymptotic region. These values could be affected by fragment alignment effects, but those are very weak for the CH_3 0_0^0 *Q* branch.

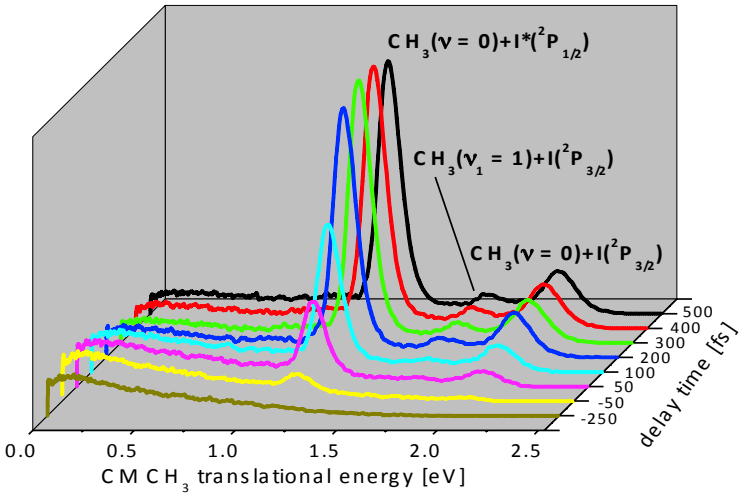

Figure 4. Center-of-mass kinetic energy distributions of CH_3 upon 266 nm photodissociation of CH_3I and a (2+1) REMPI process of methyl at 333.5 nm, which excites the vibrational components 0_0^0 and 1_1^1 of the $3p_z(^2A_2'' \leftarrow {}^2A_2'')$ Rydberg transition. The peaks correspond to the three rings in Figure 1. Vibrationless methyl is visible, formed in correlation with ground $I(^2P_{3/2})$ and spin-orbit excited $I^*(^2P_{1/2})$ fragments. Methyl with one quantum in the symmetric stretch mode ν_1=1 formed in correlation with $I(^2P_{3/2})$ is also measurable as an intermediate, weaker peak in the distributions. The results are shown as a function of the pump-probe delay time.

Of course the most appealing possibility of the time-resolved experiment with respect to the well understood nanosecond experiments is to watch the appearance of the fragments in the temporal window where they appear after parent molecule excitation. In order to determine the reaction times for the different channels, integration of each of the peaks in the kinetic energy distribution is performed at each time delay. Figure 5 shows the results obtained for the channels under study, with a more complete collection in Table 1 [34] at the end of this section. The figure shows that the main channel of this fragmentation reaction, yielding methyl and spin-orbit excited iodine, $CH_3(\nu=0)+I^*(^2P_{1/2})$, takes place in approximately 100 fs. The minor channel through the non-adiabatic surface crossing, yielding $CH_3(\nu=0)+I(^2P_{3/2})$, is complete earlier, in just 60 fs. This is expected from the higher available kinetic energy for this channel, which is translated into a larger terminal velocity and thus earlier completion. More surprisingly, the channel yielding vibrationally excited CH_3 in its symmetric stretch mode, $CH_3(\nu_1=1)+I(^2P_{3/2})$, is severely delayed, with a clocking time of around 150 fs.

It is interesting to note here that, as was noted by Zewail and others in seminal femtochemistry papers [2], the temporal resolution in this type of experiments is not limited by the duration of the pump and probe pulses (through their linear or nonlinear cross-correlation), but rather by the signal-to-noise ratio, and the reproducibility of the pulse temporal profiles. Sub-pulse duration temporal resolution is therefore not only possible, but routinely achieved with stable systems.

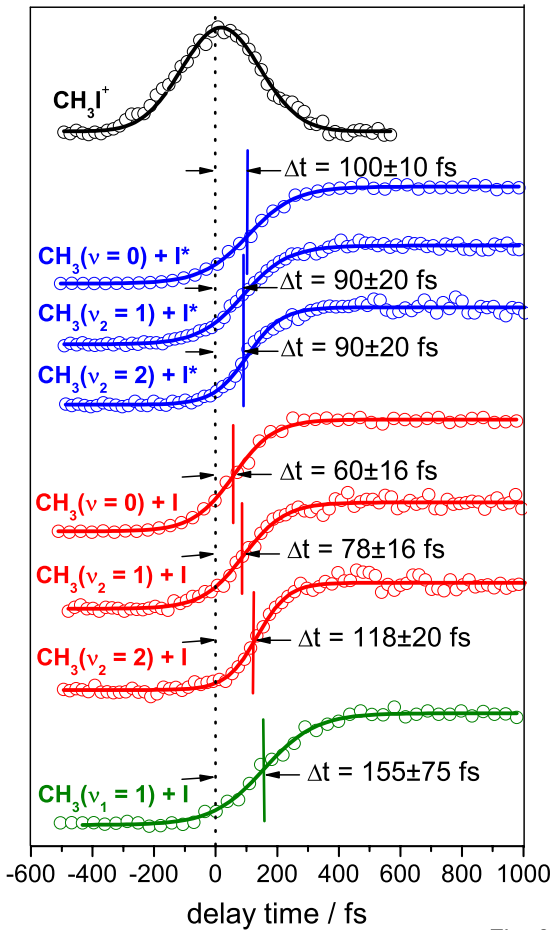

Figure 5. CH_3 transients corresponding to the dissociation channels yielding $CH_3(\nu)$ in different vibrational states (ν=0, ν_1=1, ν_2=1 and ν_2=2) in correlation with I and I*. The reaction times (with statistical uncertainties) are indicated in each transient. A transient corresponding to the parent molecule CH_3I^+ defining the time zero is also depicted.

The results shown above were obtained with a probe laser centered at 333.5 nm causing a (2+1) REMPI transition in CH_3, corresponding to the *Q* branch of the $3p_z(^2A_2'' \leftarrow ^2A_2'')$ 0_0^0 transition. Vibrationless and symmetric stretch excited methyl fragments were detected. It is well known that, upon CH_3I photolysis, the CH_3 moiety goes through a severe change in geometry, from pyramidal in the CH_3I molecule, to planar as a free fragment. As a consequence of this, an umbrella-mode (ν_2) wave packet is created in the UV photodissociation. The issue of whether C-I bond elongation precedes vibrational excitation of the methyl radical, or vice versa, could be in principle examined through the measurement of "clocking" times for different vibrational components of this wave packet. In this case, contrarily to symmetric stretch excitation, that has similar frequencies for the ground and excited $3p_z$ Rydberg state of methyl, causing the 1_1^1 transition to lie spectrally close to the 0_0^0 transition, the umbrella mode frequency is almost twice as large for the $3p_z$ Rydberg state than for the ground state. This causes a considerable blue shift in the resonance wavelength, which is beyond the probe laser bandwidth. By tuning the probe laser to 329.4 nm (2_1^1 transition), or to 325.8 nm (2_2^2 transition), vibrationally excited methyl with one (ν_2=1) or two quanta (ν_2=2) in the umbrella mode can be probed. Such an experiment was performed in the Madrid laboratory and was reported in detail in Ref. [34]. Indeed, vibrationally excited CH_3 was detected, both in pure umbrella overtones and combination bands with symmetric stretch excitation. Figure 5 also depicts the transients measured when detecting vibrationally excited methyl fragments.

The values obtained for the clocking of all the channels explored are shown in Table 1. Some of the values are consistent with arguments based solely on total available energy and final relative velocity. However, they contain an intriguing result: whereas for the adiabatic channel yielding CH_3+I*($^2P_{1/2}$) the choice of the vibrational component probed does not provoke any variation of the measured clocking time, this is noticeable not the case for the non-adiabatic channel yielding CH_3+I($^2P_{3/2}$), where, systematically, higher-lying vibrational components seem to show a "delayed" appearance time.

These experimental results have been confronted with state-of-art theoretical calculations for the CH_3I in the *A*-band [34]. A wave packet model including four degrees of freedom, namely the C–I dissociation coordinate, the I–CH_3 bending mode, the CH_3 umbrella mode, and the C−H symmetric stretch mode, has been employed to calculate the reaction times of the different dissociation channels experimentally observed. The model reproduces the experimental reaction times for the $CH_3(\nu_1,\nu_2)$+I*($^2P_{1/2}$) dissociation channels with ν_1=0 and ν_2=0,1,2, and also for the channel $CH_3(\nu_1=0,\nu_2=0)$+I($^2P_{3/2}$) with notable accuracy. The model fails, however, to predict the experimental clocking times for the $CH_3(\nu_1,\nu_2)$+I($^2P_{3/2}$) channels with (ν_1, ν_2)=(0, 1), (0, 2), and (1, 0), *i.e.*, when the CH_3 fragment produced along with spin-orbit ground state I atoms is vibrationally excited. A collection of theoretical reaction times is found in Table 1. It seems, therefore, that the presence of the non-adiabatic crossing between the $^3Q_0$ and $^1Q_1$ surfaces causes a significant difference in the birth of the methyl vibrational wave packet in a manner that a 4D model has not been able to capture. This issue remains in darkness and shows the challenging nature that these time-resolved experiments in polyatomics can pose to reduced-dimensionality theoretical treatments.

Table 1. Experimental and calculated absolute and relative appearance times for the different $CH_3(\nu_1, \nu_2)$+I*(I) dissociation channels and I/I* branching ratios. The theoretical results are obtained applying different 4D and 3D models [34].

		Experiment		
(ν_1,ν_2)	(0,0)	(0,1)	(0,2)	(1,0)
I* channel, τ_1 (fs) I channel, τ_2 (fs) τ_1 - τ_2 (fs) I/I* ratio	100 ±10 60±16 40 0.11±0.02	90±20 78±16 12 0.45±0.08	90±20 118±20 -28 1.48±0.03	155±75
		4D model		
I* channel, τ_1 (fs) I channel, τ_2 (fs) τ_1 - τ_2 (fs) I/I* ratio	95.5 59.1 36.4 0.06	97.1 59.7 37.4 2.0	100.9 60.3 40.6 127	64.4
		3D model		
I* channel, τ_1 (fs) I channel, τ_2 (fs) τ_1 - τ_2 (fs) I/I* ratio	95.6 59.1 36.5 0.07	97.1 59.8 37.3 0.94	99.8 60.6 39.2 8.78	
		3D model Ref.[4]		
I* channel, τ_1 (fs) I channel, τ_2 (fs) τ_1 - τ_2 (fs) I/I* ratio	113.8 72.8 41.0 0.07	115.6 73.7 41.9 0.76	118.5 74.7 43.8 4.83	

3.2. Transition-state imaging: the non-resonant experiment

It is interesting to discuss at this point the relevance of performing resonant ionization (versus non-resonant) in the probe step, given the broad spectral width and relatively high intensity of femtosecond pulses. To shed light on this issue, we will show an example for the *A*-band dissociation of CH_3I, described above. The methyl product formed upon the C-I bond fission is probed through ionization via two methods: resonant, (2+1) REMPI, through the *Q* branch of the ground-to-Rydberg $3p_z(^2A_2'' \leftarrow ^2A_2'')$ 0_0^0 transition with a 333.5 nm, as was described in the previous section, and non-resonant ionization with a moderate intensity ($\approx 10^{12}$ W/cm^2) 800 nm pulse.

Figure 6 shows the Abel-inverted velocity maps of CH_3 for the two experiments (non-resonant ionization in (a) and resonant (2+1) ionization in (b)) in a situation where the probe laser is located at a sufficient delay so that dissociation is complete in both cases. As can be seen in the figure, the two images bear strong resemblances, with a strong inner ring that is a reflection of the CH_3+I*($^2P_{1/2}$) channel, an external, weaker ring for the CH_3+I($^2P_{3/2}$) channel, and some intermediate structures corresponding to vibrationally excited methyl in the C-H stretch mode. It has to be noted that the overall signal intensity is considerably lower for the non-resonant experiment, even for notably higher laser intensities than in the resonant case. This is expected, due to the relatively low photon energy of the 800 nm beam, and the absence of ionization-enhancing resonances. Another important difference is the more pronounced contribution of ions with low kinetic energies that appear near the central part of the image and that are the result of competing dissociative ionization pathways. This contribution causes a decrease in contrast for the channels under study and in certain cases it may mask them beyond detection. Finally, an important consequence of the use of a non-resonant probe pulse, and one that may often be desirable, is the absence of selectivity with regards to the rovibrational components of the nascent fragments. In the case of the methyl fragment, it may quite safely be presumed that practically no selection is performed in the ionization step. Since the velocity map imaging technique allows to distinguish the degree of internal excitation through the measurement of velocities and energy conservation arguments, non-resonant probing can then be used to estimate the global energy distribution in the internal degrees of freedom of the fragments. The lack of selectivity is shown in the red curve of panel (c) of the Figure, which contains kinetic energy distributions, as broadened features when compared to the resonant experiment. The difference with the resonant case, where only vibrationless methyl fragments are observed, is particularly marked in correlation with the I channel, where vibrational population inversion occurs [35]. Under the assumption that all vibrational states of methyl have the same ionization probability by the non-resonant probe laser, this result provides a direct measurement of the nascent vibrational populations. In general, this type of experiments can be employed as a measurement of the complete internal energy content of the fragment if resolution allows it.

In seminal Femtochemistry papers [2], moderately off-resonant laser probes were identified as the key to explore the presence of transient species between reactants and products in the course of a photoinduced chemical reaction. The key idea was that an intermediate species would show transient resonances detuned from those of the parent or the products of the reaction. Therefore, details of the complete potential energy surfaces could be obtained from a collection of time-and-frequency resolved experiments. This idea was demonstrated for ICN and NaI [36,37], for instance, and was at the core of the birth of Femtochemistry as a new discipline capable of observing the intermediate stages of chemical change.

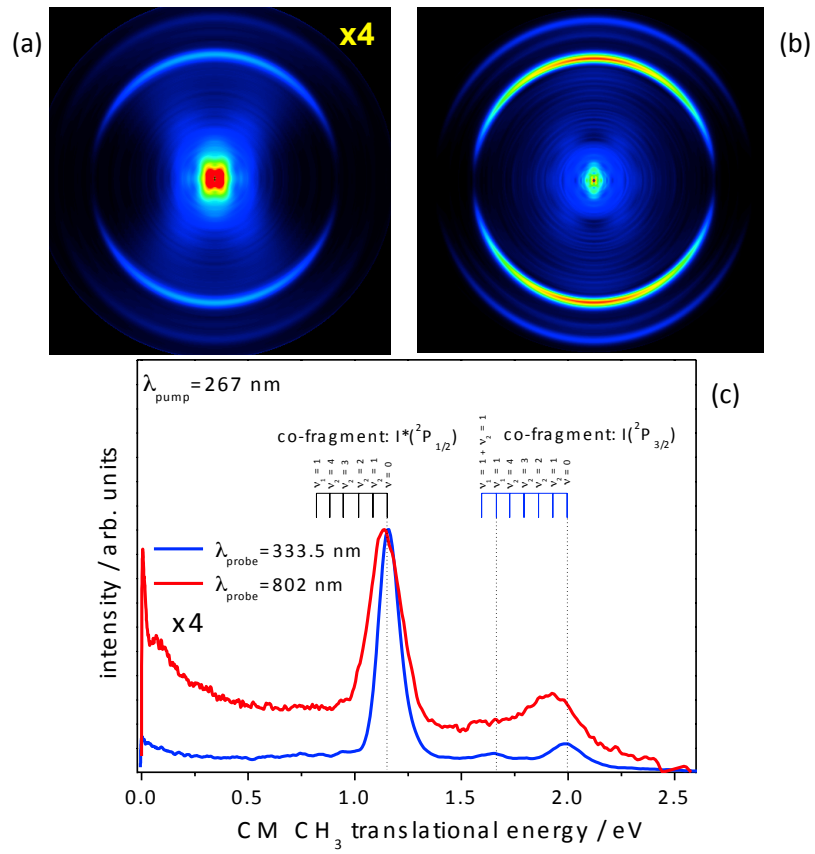

Figure 6. Abel-inverted CH_3^+ images obtained upon excitation of CH_3I at 267 nm for a pump-probe delay time of 1 ps. (a) CH_3 detection by nonresonant multiphoton ionization at 802 nm (at least seven photons are needed). The contrast of this image has been increased by a factor of 4. (b) CH_3 detection by (2+1) REMPI at 333.5 nm (*Q* branch of the $3p_z(^2A_2'' \leftarrow {}^2A_2'')$ 0_0^0 transition). (c) Asymptotic center-of-mass CH_3 kinetic energy distributions obtained at 802 nm (red) and 333.5 nm (blue) probe wavelengths together with the assignments made for the different product channels. The curves have been normalized to clarify the comparison.

A slightly different approach is presented here, where a completely off-resonance probe laser pulse is employed and information on transient species is not gained from spectral measurements, but from the recording of final kinetic energies as a function of time through the velocity map imaging technique. Figure 7 shows Abel-inverted CH_3 images as a function of the delay time between an UV pump that excites CH_3I to the *A*-band, and a near-IR probe at 800 nm. It is interesting to see how, for times immediately after time zero, intense contributions appear in the methyl ion images, that are not entirely dissimilar from those at the asymptotic limit. Analysis of the energy-angle-and-time resolved channels allowed us to propose that the measurements reflect early-time dynamics of the molecular system in the *A*-band, as will be discussed below [27,38].

The strongly enhanced signal obtained at early delay times showing a global structure with strong similarities to the asymptotic case is the main observable of this experiment. For such short times, the mechanism involves a 267 nm photon absorption in the early part of the pulse, which triggers the CH_3I *A*-band dissociation. In a fraction of molecules, the wave packet will evolve undisturbed and give rise to the neutral CH_3 and I fragments, which are amenable to be probed by a delayed 802 nm pulse at long delay times (asymptotic component). In part of the excited molecules, however, subsequent absorption of additional 267 nm photons is possible; in fact it is likely to be favoured by the presence of high-lying Rydberg states just below the ionization continuum, and only one additional 802 nm photon would be sufficient to produce CH_3I^+ in its ground state. Such (2+1') process would have a strong probability due to the resonant enhancement for the 267 nm photons

at one- and two-photon level, and the strong absorption probability of the 802 nm, which would produce the ion with little excess energy above the ionization potential.

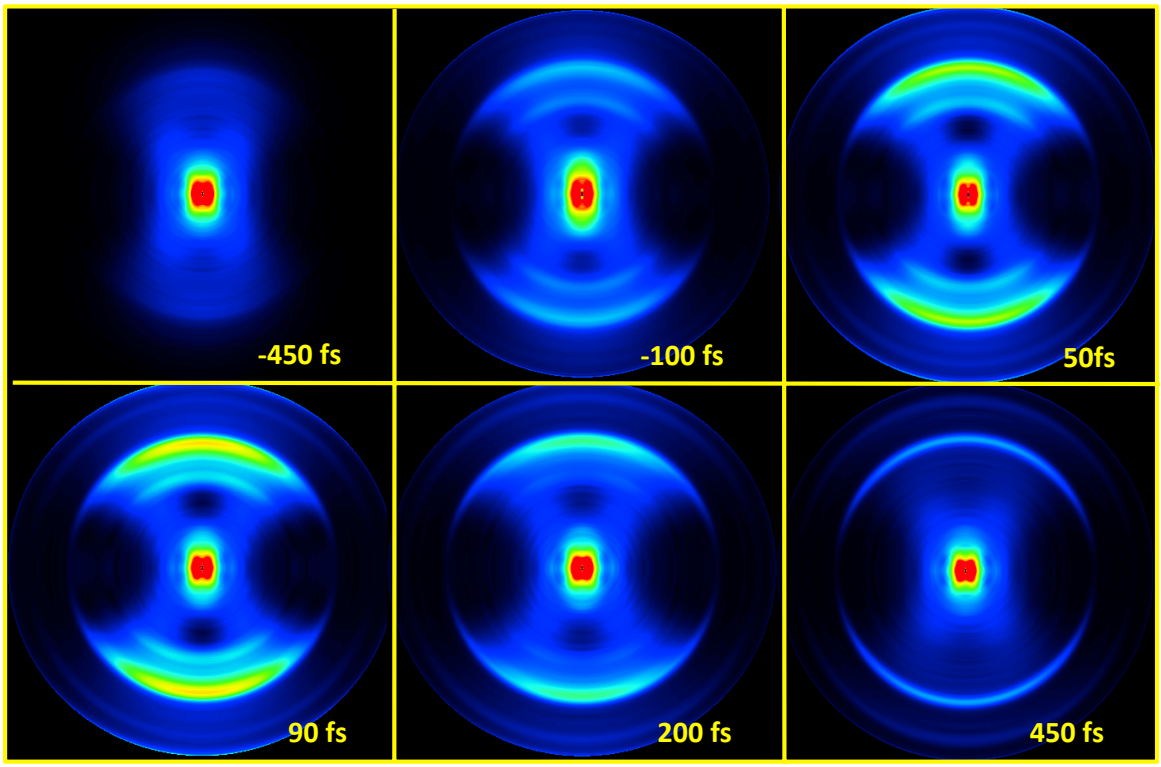

Figure 7. False-color Abel-inverted CH_3^+ images obtained as a function of pump-probe delay time. Color scale is kept constant so as to highlight the changes in overall signal intensity. The image corresponding to the asymptotic case (delay time of +450 fs) is intensified by a factor of 4 with respect to the others. The most intense ring corresponds to the main CH_3+I*($^2P_{1/2}$) dissociation channel. A larger radius ring, which produces a much weaker signal, can be attributed to the CH_3+I($^2P_{3/2}$) channel. An additional channel of lower kinetic energy (smaller radius) and strong anisotropy can be seen when pump and probe pulses overlap. The weak but clear rings that can be observed in the image taken at a delay of +450 fs corresponding to the asymptotic CH_3+I*($^2P_{1/2}$) and CH_3+I($^2P_{3/2}$) *A*-band dissociation channels keep a similar intensity for much longer delay times.

Given the very rapid dissociation in the *A*-band (~100 fs), the transient species $[CH_3\cdots I]^{\ddagger}$ can still absorb further 267 nm photons coming from the trailing edge of the pulse even for considerably elongated internuclear distances. If sufficient time has passed before absorption takes place, the wave packet on the *A*-band will have already split due to the early non-adiabatic crossing between the $^3Q_0$ and $^1Q_1$ surfaces, acquiring different excess kinetic energies. Upon simultaneous 267 nm and 802 nm absorption, it would be expected that the part of the wave packet evolving on the $^1Q_1$ surface could be promoted to the *A* excited state of CH_3I^+, which is known to undergo a fast internal conversion to the CH_3^++ I($^2P_{3/2}$) asymptote (ground state of the ion), and the part evolving on $^3Q_0$ to the *B* excited state of CH_3I^+, which would dissociate to the CH_3^++I*($^2P_{1/2}$) asymptote (see Figure 13 of Ref. [27]).

Considering this mechanism, which is very much in the spirit of the methodology presented by Zhong and Zewail in Ref. [38], the kinetic energy finally present in the methyl ion fragment should contain two contributions. The first contribution arises from the available energy of the neutral *A*-band dissociation at a given intermediate C–I

internuclear distance ($E_{av}^{\ddagger}$), which will be smaller than the asymptotic available energy (E_{av}^{final}), since the wave packet cannot have reached a very long internuclear distance at the time of the second absorption (see Figure 13 of Ref. [27]). Since the excess energy upon the ionization step will be taken by the ejected electron, the other contribution comes only from the available energy on the ionic repulsive potential surface once the wave packet has initially evolved in the neutral potential surface. The CH_3 kinetic energy shifts observed in the kinetic energy distributions shown in Figure 8 indicate that the methyl fragment carries less energy close to the temporal overlap of the pump and probe pulses than in the asymptotic region (long delay time), which can be explained if the ionic dissociative surface is flatter than the neutral surface. The fact that we observe a larger shift as the delay time is shortened is an indication that the 802 nm pulse provides the time when the wave packet is frozen in the neutral dissociation surface and taken to the flatter ionic dissociative surface, where the total energy gained is bound to be lower. The broadened kinetic energy distribution peaks measured for short delay times are also consistent with this mechanism, where excitation is produced in a region of the neutral dissociative surface of rapidly changing potential, and therefore, parts of the wave packet with a range of kinetic energies will contribute for a given delay time.

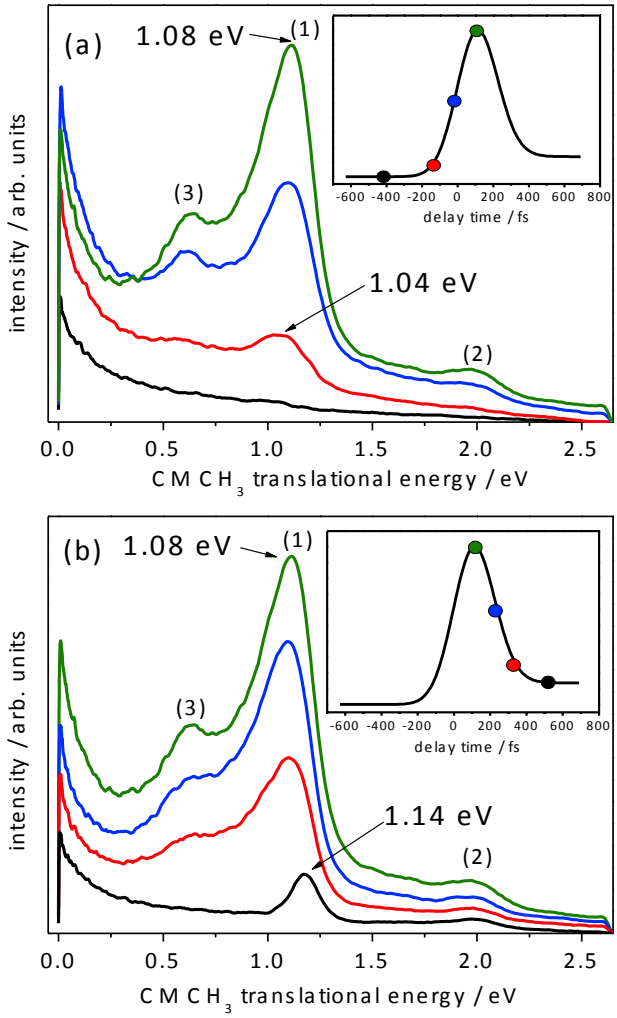

Figure 8. Center-of-mass CH_3 kinetic energy distributions at selected pump-probe delay times as indicated in the insets, where the fitted curve corresponding to the transient obtained by angular integration of the ring assigned to the CH_3+I*($^2P_{1/2}$) channel in the images of Figure 7, is depicted along with color circles to clarify what delay times are represented: (a) from -400 to 110 fs and (b) from 110 to 520 fs. Peaks (1) and (2) correspond to the CH_3+I*($^2P_{1/2}$) and CH_3+I($^2P_{3/2}$) channels, respectively. Peak (3) may correspond to a dissociative ionization channel. The labels on top of peak (1) indicate the values of the CH_3 kinetic energy at the maximum of the peak.

The above discussion shows that a strategy based on employing an off-resonant laser probe, can go beyond the idea of finding resonances in transient species, and can profit from universal ionization at sufficiently high laser intensities, coupled to a detection technique that is sensitive to the energy content of the fragments.

3.3. Observation of transient molecular alignment

A few words will be said here about the contribution of laser-induced molecular alignment to the fragment angular distributions observed in photodissociation processes. In general, any molecular system whose polarizability is not isotropic will show some tendency to align in the presence of an alternating electric field [39,40], in a process where the axis of highest polarizability will tend to align along the light polarization axis. For long pulses (pulses of longer duration than the rotational period of the molecule), molecular alignment adiabatically follows the laser pulse intensity envelope, whereas for short pulses, the molecule cannot follow the envelope and, instead, coherences are created between the rotational components that give rise to recurrences, or revivals of the molecular preferential alignment [41,42]. The two types of alignment are often termed adiabatic and impulsive alignment, respectively.

Laser-induced molecular alignment must be taken into account in all situations where the target molecule has anisotropic polarizability (as most do) and the laser intensity is high enough. In practice, typical photodissociation processes induced in the UV with moderate pulse energies are not carried out at intensities that are sufficiently high to induce an important degree of alignment. However, whenever infrared fields are added, with the purpose of inducing nonlinear effects (multiphoton absorption, Coulomb explosion, etc), the contribution of molecular alignment to the observed angular distributions cannot be disregarded as long as the intensities are of the order of 10^{12} W/cm^2 or above.

An example of the considerations above will be shown for the case of CH_3I *A*-band dissociation, through the inspection of the angular distributions of the CH_3^+ images shown in Figure 7. It is obvious simply through visual inspection that the most important contribution at times near temporal overlap between the 266 nm UV pulse and the 800 nm IR pulse is angularly narrower than the main asymptotic contribution observed at 450 fs delay. Two effects may contribute to this narrowing of the angular distribution near time zero: one is a multiphoton pump step, and the other is a dynamic alignment process of the parent molecule due to the intense 800 nm pulse [43,44]. In order to separate these effects, a further three laser pulse experiment was performed where impulsive molecular alignment was induced using an equivalent – same energy per pulse and focusing conditions – 800 nm pulse. After a controlled delay, a photodissociation experiment was performed at 266 nm, followed by an on-resonance, long delay time REMPI probing of the resulting methyl fragment (as in the resonant experiment described in the first section). Figure 9 shows the expected value of the $\cos^2\theta$ distribution for the main ring in the image, as a function of the delay between the strong IR pulse and the photolysis laser.

This result shows that indeed some degree of molecular alignment is obtained by the fact that, at around 32 ps, the first half revival of CH_3I is neatly observed, with the typical shape of angular recurrences. If molecular alignment were the only source of angular narrowing, it would be predicted that the variations at the half revival and at time zero should be of the same order. Therefore, the factor of 4 lower modulation observed at the revival time, compared to that at time zero indicates that, even though molecular alignment does play a partial role in the angular narrowing observed at time zero, the main attribution must be to

a change in the nature of the pump laser absorption from a one-photon to a multiphoton process.

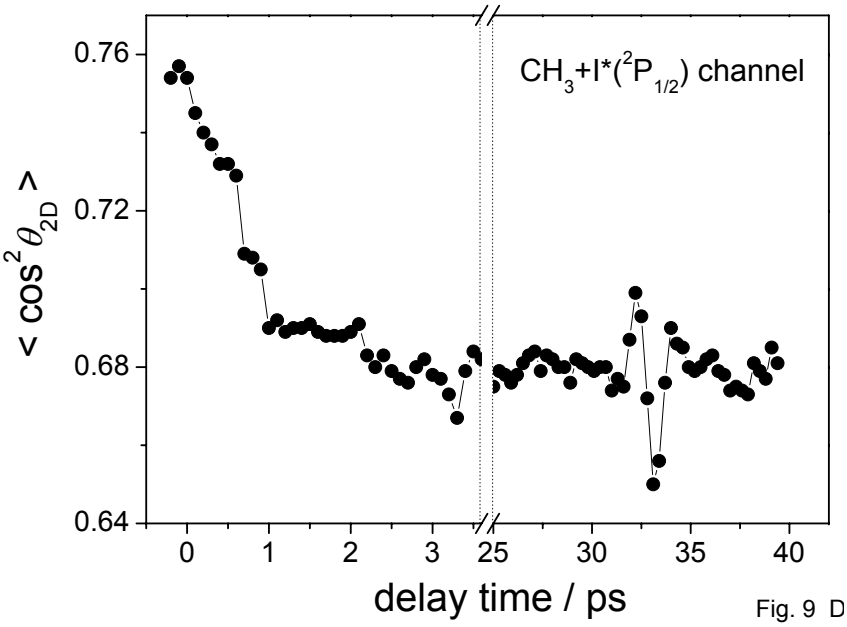

Figure 9. Alignment dynamics of CH_3I represented by $\langle\cos^2\theta_{2D}\rangle$. This quantity is derived from the intense ring in the CH_3^+ raw images assigned to the $CH_3(\nu=0)+I^*(^2P_{1/2})$ channel measured as a function of the delay time between an IR alignment pulse (802 nm) and the excitation pulse (267 nm). The $CH_3(\nu=0)$ fragment arising from the *A*-band photodissociation of CH_3I is probed at a long delay time (several picoseconds) by (2+1) REMPI at 333.5 nm. The first half revival is observed at a delay time between the alignment and photolysis pulses of ≈32 ps, which corresponds to half of the rotational period of the molecule.

3.4. $(CH_3I)_2$ dimer photodissociation dynamics

This section is devoted to the study of a fast photoinitiated process in a cluster through the use of a femtosecond laser pump–probe scheme and the detection of fragments in velocity map imaging conditions. Such work has been carried out on the $(CH_3I)_2$ system and constitutes the first report of its kind. A chronogram of the fragmentation process, with a detailed picture of the energy distribution including orientational features and the appearance times of the relevant channels will be presented here. As will be shown, it is demonstrated that cluster-specific behaviour produces crucial changes even in a prompt bond fission like *A*-band dissociation of CH_3I.

Clusters, or aggregates, offer a unique chance to study the influence of a weakly bound environment on a photoinitiated process. The ‘‘solvent’’ effect does not necessarily involve subtle changes: even though, typically, inter-molecular distances in van der Waals clusters are large, several examples exist in the literature of a phenomenon known as ‘‘concerted’’ photochemistry,[45,46] *i.e.* reaction routes that are only possible in clusters, since they involve reactions between constituent molecules. While concerted photochemistry is the most extreme case of cluster-specific chemistry, reactions that can take place in the isolated molecule can witness important differences when the molecule is immersed in such an environment. It is this type of study that has been undertaken, where the ultrafast ejection of a CH_3 group from a UV-irradiated methyl iodide dimer $(CH_3I)_2$ in the *A*-band has been analyzed and the changes with respect to the analogous process in the isolated molecule have been identified.

The expansion conditions are similar to those employed in the investigation of monomer photodissociation described above, to ensure a moderate degree of clustering, since the focus of the work is dimer dynamics, and the presence of larger clusters is undesirable. The experiment was carried out, in this case, in the middle – colder – part of the molecular beam, so that CH_3I and $(CH_3I)_2$ are the main species, with number densities of the same order of magnitude. Aggregates up to $(CH_3I)_5$ constitute a negligibly low fraction of the detected species [12].

The simultaneous presence of the monomer and the dimer has been turned to our advantage in this experiment, since the photodissociation process is amenable to study both species in only one experiment. Figure 10 shows the CH_3 images obtained using 267 nm pump (center of the CH_3I *A*-band) and 333.5 nm probe photons (for methyl detection), in monomer (Figure 10a) and cluster conditions (Figure 10b), acquired at asymptotic time delays. Figures 10c and 10d shows the corresponding center-of-mass kinetic energy distributions. As was said above, contributions related to *A*-band dissociation of both the monomer and the dimer appear on the same image, due to the simultaneous presence of both species. Comparison of Figures 10a and 10b indicates that the presence of clusters introduces three new contributions to the image. One is a broad, structureless component that can be seen approximately from 0 to ~3 eV and that can be fitted as the sum of two Gaussian distributions on the velocity axis, peaking at ~1.2 eV and ~3 eV. The other two are two new rings (peaks 1' and 2' in Figure 10d), which appear at lower kinetic energies compared with those of the monomer (peaks 1 and 2 in Figure 10d), broadened in energy and with a larger ratio between the high kinetic energy component ($I(^2P_{3/2})$ channel in the monomer) and the low kinetic energy component ($I^*(^2P_{1/2})$ channel in the monomer).

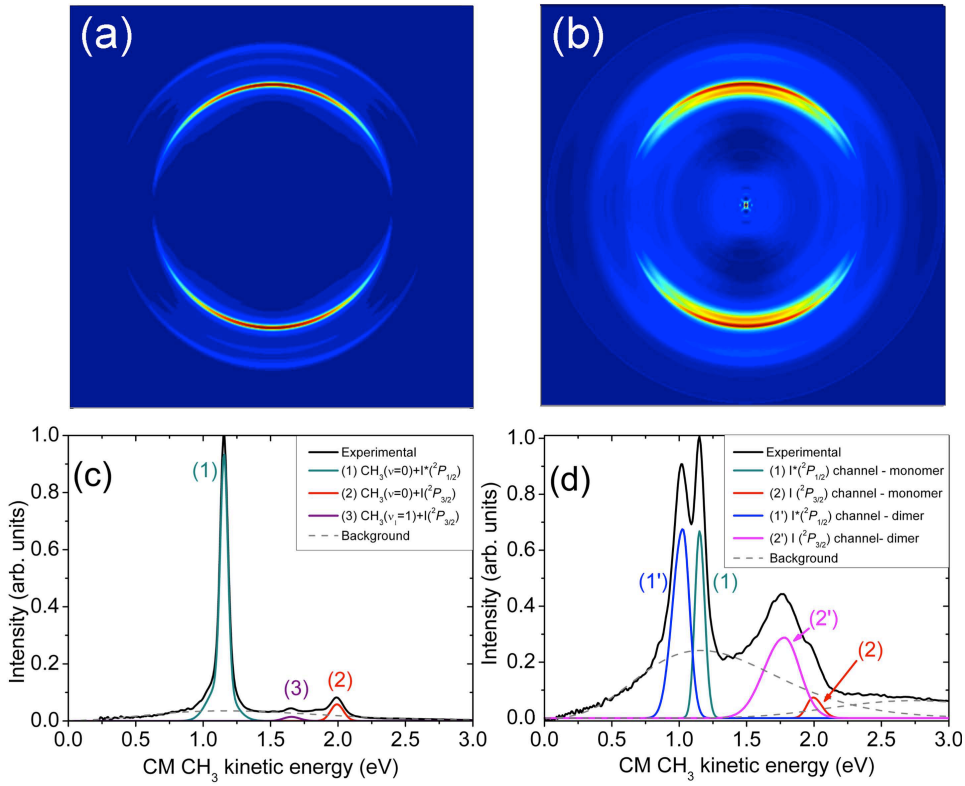

Figure 10. (a) and (b) Abel inverted experimental CH_3^+ images obtained upon excitation of (a) CH_3I, and (b) a mixture of CH_3I and $(CH_3I)_2$, by two laser pulses: pump pulse at 267 nm and probe pulse, delayed by 1.5 ps, at 333.5 nm, for CH_3 (2+1) REMPI. (c) and (d) Corresponding center-of-mass kinetic energy distributions of CH_3. Experimental data are shown together with simulated curves for the several contributions observed. The separate pump and probe laser contributions have been subtracted from the total signal in both the images and kinetic energy distributions.

For the low kinetic energy channel, the contributions from the monomer and dimer are clearly distinguishable, but this is no longer the case for the high kinetic energy channel, which appears very significantly broadened and more intense, so much that the monomer $I(^2P_{3/2})$ channel only appears as a shoulder in the high kinetic energy area of the dimer peak. The weaker $CH_3(\nu_1=1)+I(^2P_{3/2})$ channel (see section on *A*-band photodissociation) can no longer be observed in these conditions.

The experimental observations point to the idea that the two new rings observed in the CH_3^+ images correspond to *A*-band dissociation of the $(CH_3I)_2$ dimer, where the CH_3 fragment is formed in correlation with either the $[I\cdots CH_3I]$ species (high kinetic energy contribution) or the $[I^*\cdots CH_3I]$ species (low kinetic energy contribution). In this scenario, we will refer to the "$I(^2P_{3/2})$ channel" and the "$I^*(^2P_{1/2})$ channel" when describing dimer dissociation.

A-band dissociation in the dimer can appear modified for several reasons, the stabilization energy in the dimer and the different degree of rotational excitation in the outgoing fragments being the most obvious causes of change. The reduction in the kinetic energy of the CH_3 fragment in correlation with $I^*(^2P_{1/2})$ observed in this work is 0.12±0.01 eV, which would correspond, in the absence of other effects, to a decrease in the total available energy of 0.13 eV. In the $I(^2P_{3/2})$ channel, we observe a shift of 0.20±0.04 eV. As to the effect of rotation, it is clear from the larger energy width of the peaks associated with dimer dissociation that a significantly larger degree of rotational excitation is present, while no distinction can be made as to whether it corresponds to the light outgoing CH_3 fragment or to the $[I/I^*\cdots ICH_3]$ co-fragment, as both imply a reduction of the total available kinetic energy.

In combination with *ab initio* calculations [12] that have produced optimized geometries for the dimer and energy values and oscillator strengths for the excited states of the *A* band of $(CH_3I)_2$, these results have provided solid understanding of the blue-shift of the *A*-band in the $(CH_3I)_2$ dimer. This shift had been reported previously and had been qualitatively understood in terms of the ground state dimer being stabilized by a dipole–dipole interaction, while the molecular dipole is weakened by the valence state transition, which involves the promotion of an electron located mainly on the I atom to an antibonding molecular orbital. With a lower dipole–dipole interaction, the dimer in the valence state will not be as stabilized as in the ground electronic state. Donaldson *et al*. [47] reported an experimental shift of the peak of the absorption band by around 500–1000 cm^{-1} in conditions of dimer formation with respect to monomer-only conditions. This value is compatible with the value of about 0.2 eV (1600 cm^{-1}) found here.

In addition, a significant difference in the anisotropy observed for the monomer and dimer must be noted. Through the use of the multidimensional fit procedure described in the methodology section, it has been possible to discriminate the angular character of the different contributions, with the finding that, for the $I^*(^2P_{1/2})$ channel, no loss of orientational preference happens upon dimerization, and this is in contrast with the $I(^2P_{3/2})$ channel, which shows a pronounced decrease in the observed anisotropy. The implications of this observation will be discussed below.

One more feature marks a difference between monomer and dimer dissociation results in the asymptotic situation: the dramatic increase in the $I(^2P_{3/2})/I^*(^2P_{1/2})$ ratio observed through the $CH_3(\nu=0)$ fragment, from values of 0.14±0.05 for the monomer to 0.72±0.05 for the dimer. Analogous measurements were performed by tuning the probe laser to 329.5 nm and 325.8 nm, which constitute a resonant probe of $CH_3(\nu_2=1)$ and $CH_3(\nu_2=2)$,

respectively (ν_2 being the umbrella mode of CH_3). A dramatic change of the I($^2P_{3/2}$)/ I*($^2P_{1/2}$) ratio, in the same direction as that just described for $CH_3(\nu=0)$, was also observed in both cases.

The decrease of the anisotropy of the I($^2P_{3/2}$) channel in the dimer and the large change in the branching ratio need to be discussed conjointly. An increase of the I($^2P_{3/2}$)/I*($^2P_{1/2}$) ratio could be related to either a change in the main absorbing states or in the efficiency of the coupling in the non-adiabatic crossing. Since the other possibly participating states, $^1Q_1$ and $^3Q_1$, are of perpendicular nature, in contrast to the parallel $^3Q_0$ state, an examination of the change in anisotropy should permit the distinction between the two phenomena. If we consider that the I($^2P_{3/2}$) fragment observed is originated partly through absorption to $^3Q_0$ followed by crossing to $^1Q_1$, and partly through direct absorption to one of the perpendicular states ($^3Q_1$ or $^1Q_1$), then the resulting anisotropy is expected to reflect a mixture of parallel (β=2) and perpendicular (β=-1) character. From the observation of experimental values for the β anisotropy parameter, a ratio of approximately 2:1 is extracted for those two routes. This is an important result, since it indicates that the participation of absorption of the perpendicular states is not negligible, as was the case for the monomer at 267 nm excitation; instead, it accounts for approximately 1/3 of the total absorption at this wavelength. However, this alone cannot account for an increase in the I($^2P_{3/2}$)/I*($^2P_{1/2}$) ratio from 0.14±0.05 for the monomer to 0.72±0.05 for the dimer. From the combined values of ratios and anisotropy, we conclude that the efficiency of the non-adiabatic crossing approximately doubles in the dimer with respect to the monomer.

The experimental results presented above show the richness of the information that can be obtained in relatively simple experiments. In this case, through a global approach where velocities and anisotropies are examined simultaneously, detailed information on the stabilization energy, the degree of internal energy content, the contribution of several electronic excited states to the overall absorption, and finally, the effect of dimerization on the population transfer through the non-adiabatic crossing, has been obtained.

3.5. Resonant probing: the role of the optical coupling window

$(CH_3I)_2$ dimer photodissociation will be explored temporally in this section to illustrate an important feature of resonantly probed "clocking" experiments. Figure 11 shows the time evolution in the detection of CH_3 coming from the monomer in the I*($^2P_{1/2}$) channel, and also from the dimer in both the I($^2P_{3/2}$) and I*($^2P_{1/2}$) channels. The time delay for free CH_3 observation is still short in the dimer (~220 fs), but clearly delayed with respect to monomer dissociation (~80 fs). If the decrease in available energy, due to the blue shift of the band, is taken into account, calculated delays of only ~10 fs are obtained classically, indicating that this is clearly insufficient to explain the experimental measurement.

As is described in detail in Ref. [12], this case is a particularly illuminating example of the role of the probing step. In particular, it must be noted that resonant CH_3 probing is done here through a (2+1) REMPI process via a Rydberg state. This is a state of spatially extended character, and during the first phases of dissociation, it is situated in the vicinity of the [I···ICH_3] moiety, where close-lying Rydberg states can be present. In this situation, the resonance can be significantly perturbed by the nearby presence of [I···ICH_3], so that the CH_3 radical would only appear as ‘‘free’’ after an elongated distance (*i.e.* time).

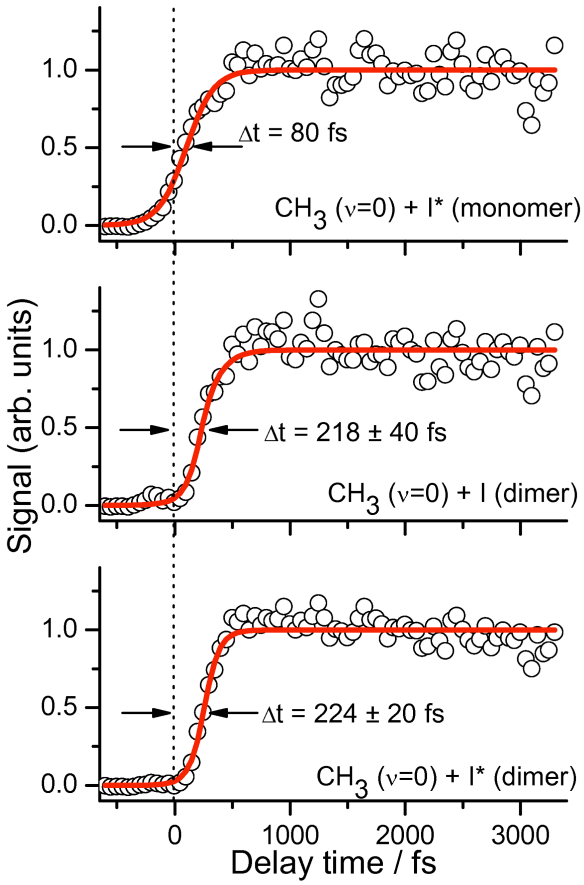

Figure 11. Transients showing appearance times of the observed channels yielding $CH_3(\nu=0)$ for both monomer CH_3I and cluster $(CH_3I)_2$ species. Open circles show the amplitudes of each of the contributions; solid lines show the fitted curves.

A simplified theoretical simulation was performed in order to assess that the delay in the measured clocking time was not due to an intrinsic difference in the photodissociation dynamics in the dimer with respect to the monomer, but to an important difference in the probing step (through the late opening of the optical coupling window) due to the extended character of the orbitals. A CASSCF calculation was performed to describe the effect of the nearby presence of the $[I\cdots ICH_3]$ species on the Rydberg electronic states of the ejected CH_3 group. A reduced model was employed for this purpose, where only two CH_3 groups are considered. The energy of the Rydberg $3p_z$ state was calculated as a function of the distance between the two CH_3 groups. A potential energy curve was obtained that shows significant distortion for elongated distances. This necessarily implies that the optical window for the REMPI transition employed to detect the appearance of the CH_3 fragment will not be open until the distance is sufficiently long so that this distortion is negligible (at least, of the order of the bandwidth of the probe laser). A classical 1D dynamic calculation was performed under the simplification that the CH_3 dynamics takes place on the $^3Q_0$ monomer surface (shifted by 0.12 eV to account for the blue shift of the band), but the probe laser absorption could only take place once the $3p_z(^2A_2'' \leftarrow {}^2A_2'')\ 0_0^0$ transition in CH_3 became resonant under the influence of the nearby presence of the other CH_3. For the estimation of the distances CH_3–CH_3, an axial CH_3–I recoil and a head-tail geometry for the cluster were assumed. This calculation produced a delay of ~80 fs for the $I^*(^2P_{1/2})$ channel with respect to the situation where distortion of the Rydberg state of CH_3 does not occur. Even though this is somewhat shorter than the experimental delay (~140

fs), it is clearly of the same order of magnitude, and we believe this is the main mechanism producing a delay in the apparent dissociation times for the dimer. We consider that this is a clear illustration of the fact that this effect, where a substantial delay occurs in the time opening of the optical detection window, needs to be taken into account whenever resonant probing is employed, especially for large molecules, and in particular clusters, where intermediate orbitals used for the resonant transition can be substantially modified by the nearby presence of a similar moiety.

The time-resolved work performed on the $(CH_3I)_2$ species shows that even the influence of a weakly bound environment can have profound influences on a molecular dissociation process. The phenomenon that was chosen (fast ejection of a CH_3 fragment from a $(CH_3I)_2$ dimer) would not seem prone to showing this effect, due to the extremely fast nature of the dissociation and the weak bond between the two CH_3I molecules. Nevertheless, dramatic changes both in the absorbing states and in the strength of non-adiabatic couplings between them have been detected. It is expected that these cluster related effects will be even more important in slower processes and more tightly bound systems.

4. THE *B* BAND

The second absorption band in methyl iodide, the *B* band, has been by far much less studied than the more accessible A-band. It starts at around 200 nm and hence, the possibility of performing detailed spectroscopic studies with conventional lasers is restricted to the red edge of the band. The *B* band results from the excitation of a $5p\pi$ electron of the I atom to a 6*s* molecular Rydberg orbital. The remaining three $5p\pi$ electrons are subject to strong spin-orbit coupling, so that, in C_{3v} symmetry, the ionic core can be in the $^2\Pi_{3/2}$ ($^2E_{3/2}$) or the $^2\Pi_{1/2}$ ($^2E_{1/2}$) states. From the *J-j* coupling between the ionic core states and the Rydberg electron several bound states are formed. Transitions to those related with the $^2\Pi_{3/2}$ ($^2E_{3/2}$) core, from the ground state, constitute the *B* band, of perpendicular character. Discrete vibrational structure appears in the spectrum [47-51], but the lines are considerably lifetime broadened due to interaction with dissociative surfaces that belong to the *A* band, which causes electronic predissociation. Lifetimes of these states are in the picosecond regime and are strongly dependent on vibrational excitation in a non monotonic manner [48].

The characteristics of *B*-band predissociation in CH_3I, including lifetimes, anisotropy, branching ratio, and vibrational activity of the methyl fragments, have proven to be strongly dependent on the vibrational level of initial excitation in the parent molecule. The extreme sensitivity to the vibrational excitation is related to the details of the crossings between the potential energy surfaces and the spatial distributions of the wave functions at each vibrational level. Therefore, systematic measurements of the properties of this predissociation process provide challenging constraints for the theoretical description of this system. Here, we will briefly show the results obtained for three cases: the 0_0^0 transition at 201.2 nm (excitation to the vibrationless level of the Rydberg state), the 2_0^1 transition at 196.7 nm (one quantum of excitation in the umbrella mode), and the 3_0^1 transition at 199.2 nm (one quantum of excitation in the C-I stretch mode). Given the large spectral separation between these features (larger, in any case, than the laser bandwidth), the eigenstate picture is useful, providing that a vibronic wave packet cannot be formed.

A complete study was carried out on this system, through the time-resolved measurements of the parent ion yield, velocity map images of both the CH_3 and I fragments, obtained both with REMPI and non-resonant ionization schemes, and

photoelectron imaging detection. The complete results were published in Refs. [8,11], so here we will only review the most salient features.

4.1. Parent ion detection

The CH_3I parent decay time was measured by acquiring collections of mass-selected images as a function of delay time between the pump and the probe laser pulses. Ionization of the parent CH_3I was produced through a (1+1′) REMPI scheme. Figure 12 shows transients of the CH_3I^+ signal obtained for excitation at 201.2 nm (0_0^0 band), 196.7 nm (2_0^1 band), and 199.2 nm (3_0^1 band) and photoionization with a single photon of 304.5 nm. The measured lifetimes, τ, obtained through these transients, are 1.50±0.10 ps, 0.80±0.10 ps, and 4.33±0.20 ps, respectively. As previously announced, lifetimes change drastically depending on the vibronic level and therefore on the pump wavelength.

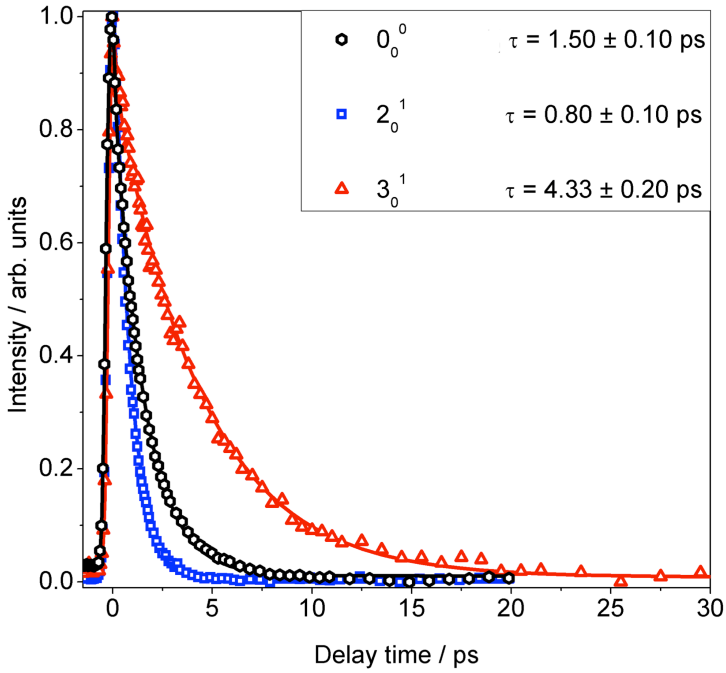

Figure 12. Experimental transients corresponding to parent CH_3I decay after 201.2 nm (black circles, 0_0^0 band), 196.7 nm (blue squares, 2_0^1 band) and 199.2 nm (red triangles, 3_0^1 band) *B*-band excitation. Probe center wavelength was 304.5 nm. Solid lines correspond to the fit of the experimental data.

4.2. Fragment velocity map imaging detection

Fragment detection (I and CH_3) was performed in velocity map imaging conditions, as a function of the delay between the pump laser pulse and the ionizing-probe pulse. Figure 13 shows an example of such measurement, where methyl images were acquired for a series of time delays after CH_3I excitation in the 2_0^1 transition of the *B*-band.

It is interesting to note that, contrarily to the dynamics expected for the *A*-band, caused by a prompt bond fission, in this case the appearance of the methyl fragment is mediated by a finite state lifetime, and therefore, transient behavior is expected to follow an exponential function of the form

$$S(t) \propto e^{-4\ln 2\left(\frac{t}{\tau_{CC}}\right)^2} \otimes [(1-e^{-\frac{t}{\tau}}) \times H(t)] \qquad (8)$$

where τ is the lifetime of the initial state and τ_{cc} is the instrumental response time. It can be argued that such behavior should be temporally shifted due to the additional dissociation time along the dissociative surface. It has not been considered here because this time is negligible when compared to predissociation times in this case. Fits of the parameters in Eq. (8) to the integrals of the contributions visible in Figure 13 provide lifetimes compatible with those obtained from parent ion yields.

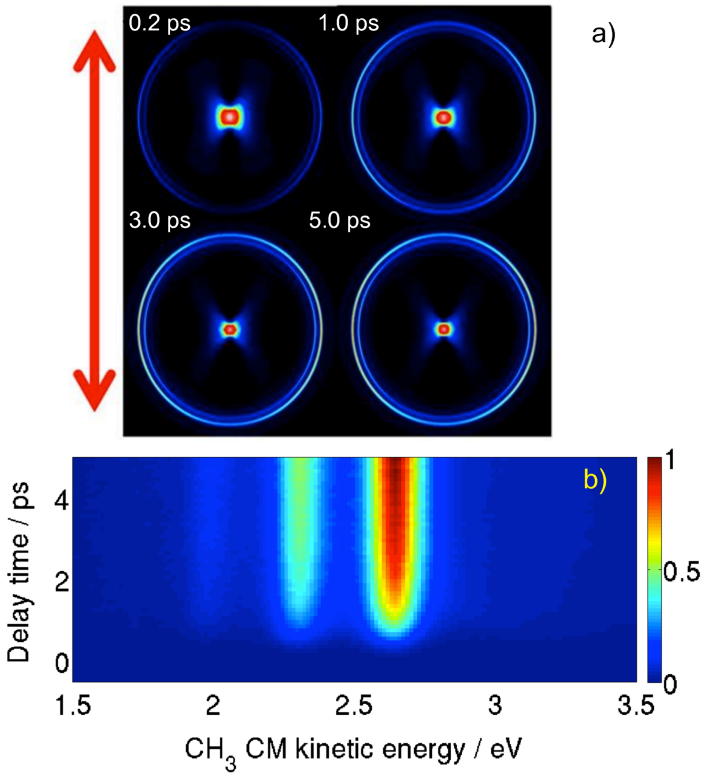

Figure 13. (a) Sequence of Abel-inverted methyl images, in false color, for a pump-probe delay time of 0.2, 1, 3, and 5 ps for a pump laser center wavelength of 196.7 nm for *B*-band excitation of CH_3I to the 2_0^1 vibronic level and a probe laser center wavelength of 333.5 nm. The double-sided arrow indicates the polarization axes of both lasers. (b) 2D map of the kinetic energy distribution of the CH_3 fragment as a function of the delay time.

As shown above for the *A*-band section, fragment detection with short pulses can be achieved via resonantly enhanced ionization schemes, or via non-resonant strong IR field ionization. In some cases, the application of this double approach allows to obtain estimates of product state distributions. We will show an example here. Figure 14a, shows asymptotic kinetic energy distributions for the methyl fragment formed in *B*-band predissociation of methyl iodide in the 2_0^1 band. The three curves correspond to the detection of methyl in its vibrationless state (0_0^0, purple curve, at 333.5 nm), one quantum in the umbrella mode (2_1^1, red curve, at 329.4 nm) and two quanta in the umbrella mode (2_2^2, blue curve, at 325.8 nm). Excitation of the symmetric stretch mode is observed simultaneously. The open circles in Figure 14b contain the methyl fragment kinetic energy distribution obtained though non-resonant IR ionization. Under the assumption of similar ionization probabilities under the IR field, obtaining the best multiplicative factors for the resonant curves to fit the non-resonant curve yields estimates of nascent vibrational components of the methyl fragment [8]. As an example, Figure 15 shows the relative vibrational populations extracted from the above mentioned analysis corresponding to the stretching mode excitation of the methyl fragment for the different initial vibrational states excited in the Rydberg state. The increasing vibrational activity in this mode is evident when moving from the 0_0^0 to 2_0^1 to 3_0^1 transitions.

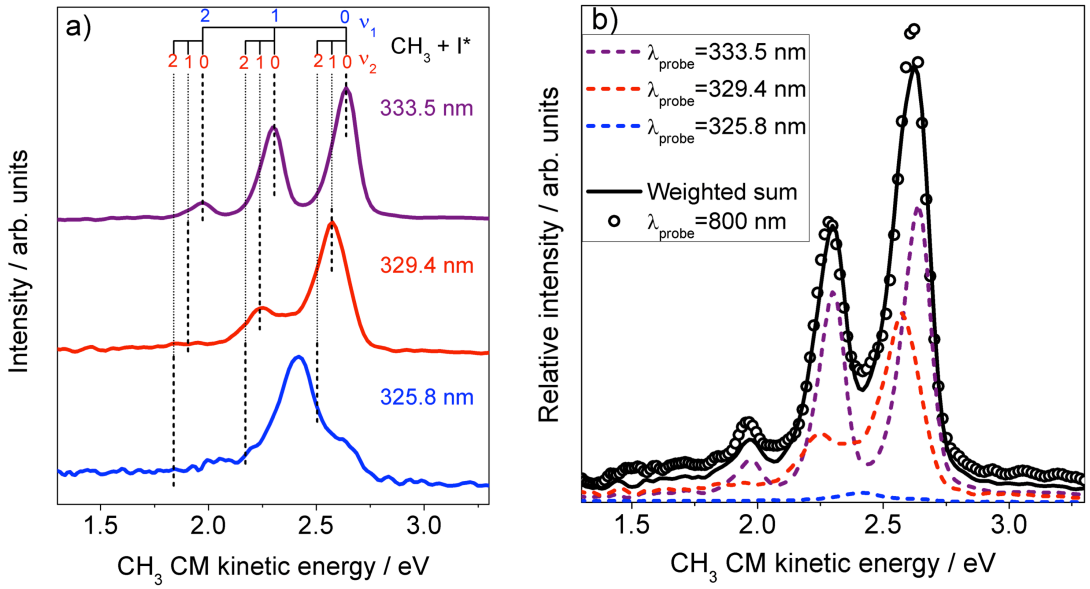

Figure 14. (a) Center-of-mass CH_3 kinetic energy distributions measured at a pump-probe delay time of 10 ps, with a pump laser centered at 196.7 nm for *B*-band excitation of CH_3I to the 2_0^1 vibronic level and a probe laser centered at 333.5 nm (top), 329.4 nm (middle), and 325.8 nm (bottom), in resonance with the *Q* branch of the two-photon $3p_z(^2A_2'' \leftarrow {}^2A_2'')$ transition in CH_3 in its 0_0^0, 2_1^1, or 2_2^2 bands, respectively. (b) Center-of-mass CH_3 kinetic energy distribution upon *B*-band excitation of CH_3I at 196.7 nm to the 2_0^1 vibronic level and subsequent CH_3 non-resonant multiphoton ionization probing with pulses centered at ≈800 nm delayed by 10 ps (open circles). Colored lines contain the resonant probing distributions shown in the left panel, at 333.5 nm (dashed purple), 329.4 nm (dashed red), and 325.8 nm (dashed blue). The solid black line is the distribution obtained through the weighted sum of the three kinetic energy distributions for resonant CH_3 probing.

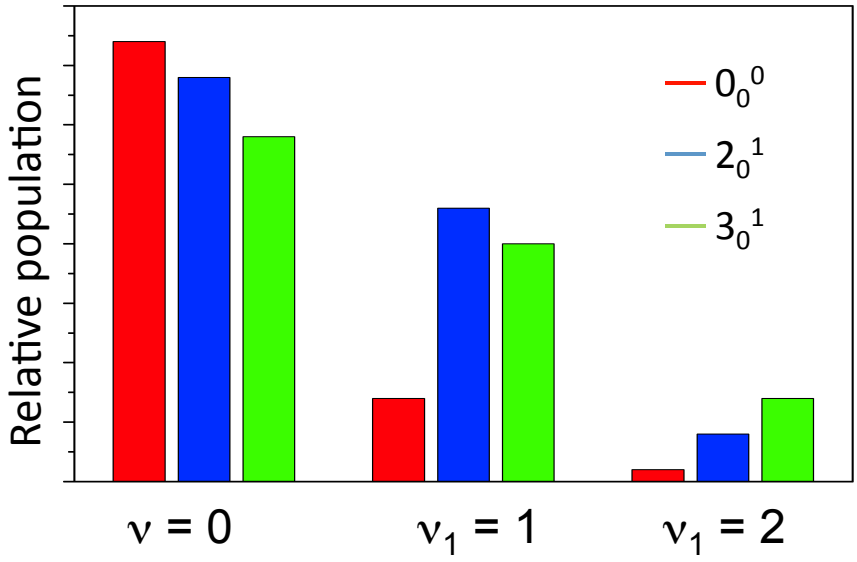

Figure15. Relative vibrational populations extracted from the fit of the data shown in Figure 14 for the stretching mode of the methyl fragment arising from predissociation at the 0_0^0, 2_0^1 and 3_0^1 levels.

It is interesting to note that the time-resolved velocity map imaging technique allows to monitoring changes in the anisotropy of the fragment angular distribution as a function of time, and thus, in the absence of fragment alignment effects, it provides information on molecular rotation. This phenomenon has been explored for the *B*-band through detection of the $I^*(^2P_{1/2})$ fragment, which does not show alignment effects, because the populations of the M_J=±1/2 must be equal [8,52], so that its angular distribution is a reflection of parent molecular rotation.

The results of time-resolved I*($^2P_{1/2}$) detection can be seen in Figure 16. The left panel shows iodine ion images as a function of time for the 2_0^1 transition of the CH_3I *B*-band. The first image, taken at 200 fs delay, shows extreme perpendicular character, with β ~ -1, reflecting the perpendicular nature of the transition. Iodine ions are thus concentrated in the equator of the sphere whose poles are defined by the polarization vector of the pump laser beam. Measuring iodine at later times shows a relaxation of this extreme anisotropy, that is, a significant number of iodine atoms appear along the poles of the sphere described above. The variation of the β parameter, defined in Eq. (1), as a function of time is shown quantitatively in the right panel of Figure 16. The temporal scales of the anisotropy change are related to the lifetime of the excited state, and also to the degree of rotational excitation in the parent molecule [8]. From semiclassical models, rotational temperatures of ~40 K are expected to account for the measured values [53,54].

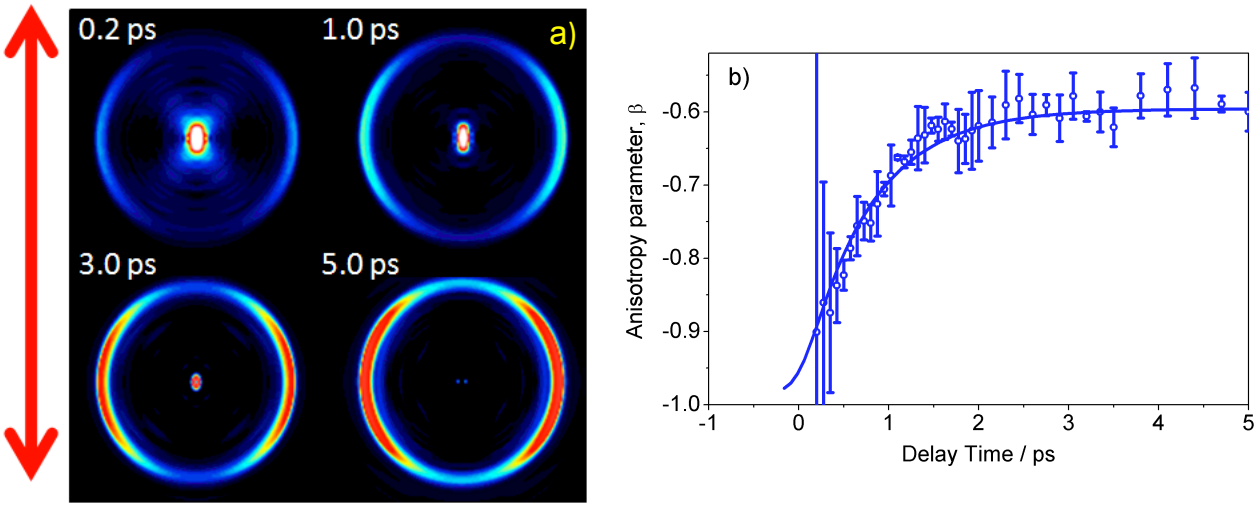

Figure 16. (a) Sequence of Abel-inverted iodine images, in false color, for a pump-probe delay time of 0.2, 1, 3, and 5 ps for a pump laser center wavelength of 196.7 nm and a probe laser center wavelength of 304.5 nm. The double-sided arrow indicates the polarization axis of both lasers. (b) Experimental anisotropy transient corresponding to I*($^2P_{1/2}$) appearance after 196.7 nm *B*-band excitation of CH_3I to the 2_0^1 vibronic level. Error bars correspond to the standard deviation of each point obtained from the set of experimental runs.

4.3. Time-resolved photoelectron imaging

Time-resolved photoelectron velocity map imaging experiments provide additional information on the process. In this case, a pump-probe scheme has been found that allows the detection of photoelectrons originated by ionization of the parent in the excited Rydberg state (at short delay times), or those originated by REMPI of the iodine atom born after the molecule breaks (for long delays). For intermediate delays, both signals are present simultaneously and can be separated through their kinetic energies. This was achieved through a pump-probe scheme where the pump beam is centered at the desired *B*-band transition of the molecule, and the probe beam causes REMPI ionization in the product. In this manner, photoelectrons originated from ionization of the parent are created in a (1+1') process, and those originated in the iodine fragment are caused by a (1+2'+1') process, where the first photon excites the parent molecule, and the subsequent (2'+1') process occurs in the free fragment. This is shown in Figure 17, where the results corresponding to the 0_0^0 and 3_0^1 bands are shown in the left and right panels, respectively. In both cases, the photoelectron rings that appear most intense for short delays gradually become dimmer, with the time constant of the molecular predissociation, and the higher-

radius rings due to ionization of the iodine product grow in intensity until they reach their final value, with a time constant consistent with the former. It is interesting to note that only photoelectrons due to the ionization of the iodine atom product, but not to the methyl product, are detectable, since iodine ionization is strongly enhanced due to the use of a REMPI scheme.

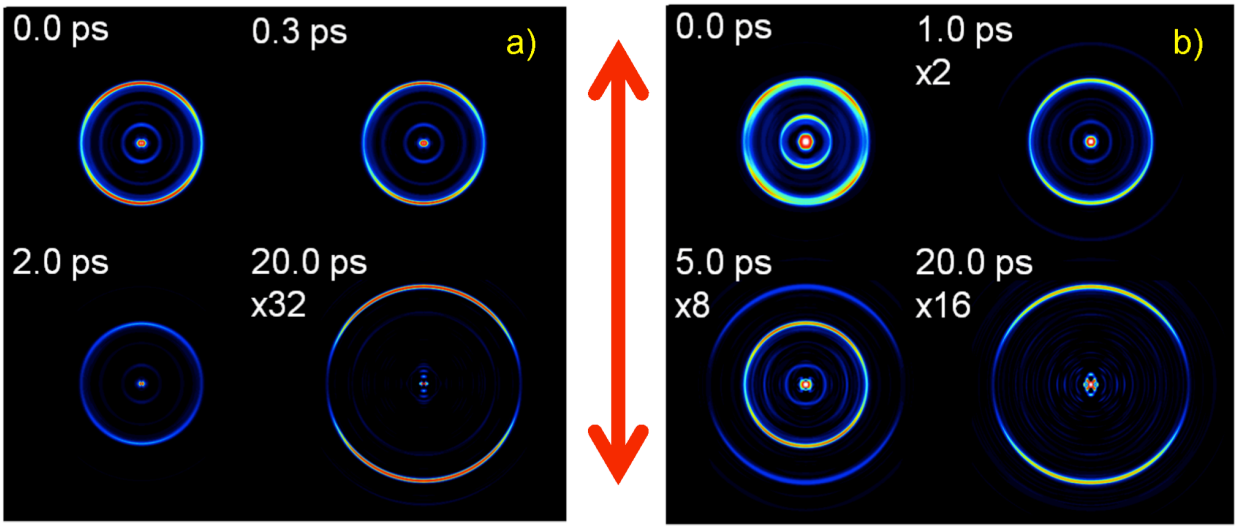

Figure 17. Left: Sequence ~of Abel-inverted photoelectron images, in false color, for a pump-probe delay time of 0, 0.3, 2, and 20 ps for a pump laser center wavelength of 201.2 nm (000 band) and a probe laser center wavelength of 304.5 nm. The double-sided arrow indicates the polarization axis of both lasers. Right: Sequence of Abel-inverted photoelectron images, in false color, for a pump-probe delay time of 0, 1, 5, and 20 ps for a pump laser center wavelength of 199.2 nm (3_0^1 band) and a probe laser center wavelength of 304.5 nm. The double-sided arrow indicates the polarization axis of both lasers.

Photoelectron spectra obtained through angular integration of the rings in Figure 17 are shown in Figure 18 for early (top panels) and late times (bottom panels) for the 0_0^0 band (left panels) and the 3_0^1 band (right panels). In each case, they are plotted as a function of the binding energy of the corresponding species. The photoelectron spectra provide information on the initial molecular excitation, and in that sense, the results shown in panel (b) of Figure 18 constitute a confirmation that the initial excitation is almost exclusively to the ν_3=1 state. Since the potential energy surface of the *B* 6s[2] Rydberg state is similar to the ground state surface of the ion, transitions with Δv=0 are expected to dominate [51,55] and, therefore, the main contribution is related to the formation of CH_3I^+ with one quantum of excitation in the ν_3 mode due to initial excitation to the ν_3=1 level of the Rydberg state. Other vibrational combinations are visible in the spectrum, but always with at least one quantum of excitation in the ν_3 mode.

As mentioned before, when acquired with a long delay time between the pump and probe laser pulses, the photoelectrons are originated from the iodine atoms resulting from dissociation. Due to the pulse bandwidth, the (2+1) REMPI schemes at 304.5 nm employed are resonant for both I and I*. Evidence for I* formation is clear for both the 0_0^0 and the 3_0^1 bands; the data also suggest the minor presence of ground state iodine, which shows as a shoulder to the main I* contribution.

The combination of parent, fragment and photoelectron detection in velocity map imaging conditions, and using femtosecond pump-probe schemes with resonant and non-resonant ionization constitutes a powerful tool that can reveal the details of complex photoinduced processes, as has been shown for this case of *B*-band predissociation of CH_3I. In this case, we have measured the rapidly varying lifetimes of the vibronic states in the *B*-band,

the time dependent fragment anisotropies, the internal energy content of the fragments, and we have identified new channels that had been overlooked in the past, in particular one yielding ground state iodine, and a fast channel producing spin-orbit excited iodine through direct absorption to dissociative surfaces [8].

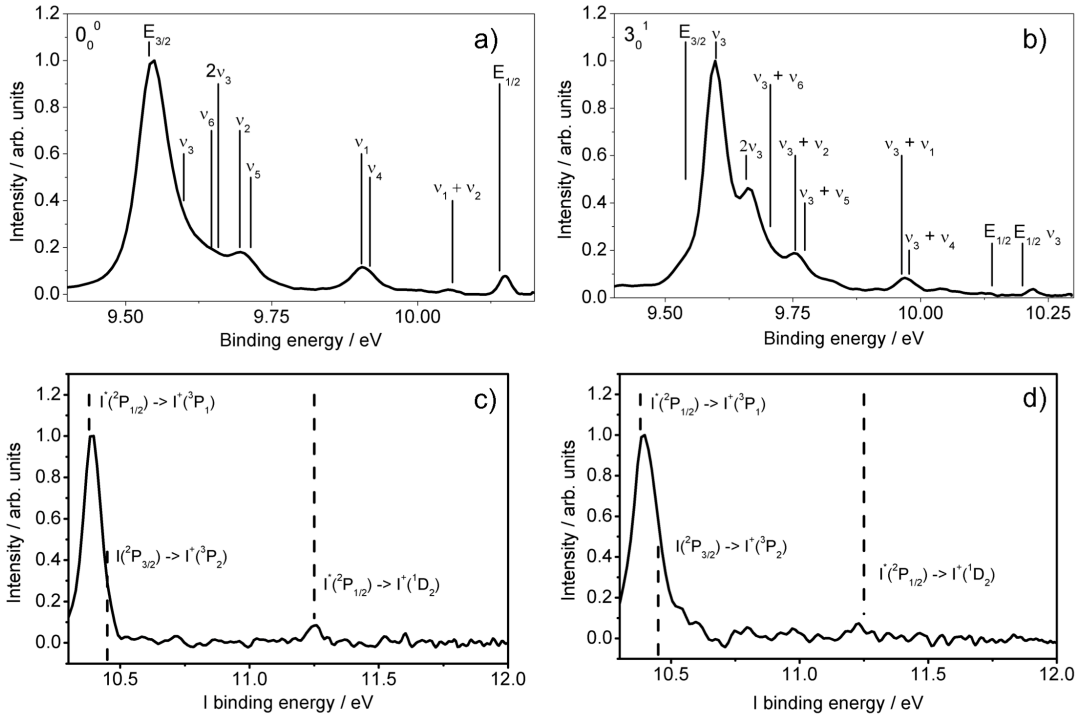

Figure 18. Photoelectron spectra plotted relative to the binding energy. Top row: Pump-probe delay time of 400 fs (photoelectron kinetic energy distribution plotted as a function of the binding energy for the parent molecule). (a) Pump laser center wavelength of 201.2 nm (0_0^0 band). (b) Pump laser center wavelength of 199.2 nm (3_0^1 band). Bottom row: Pump-probe delay time of 30 ps (photoelectron kinetic energy distribution plotted as a function of the binding energy in the iodine product). (c) Pump laser center wavelength of 201.2 nm (0_0^0 band). (d) Pump laser center wavelength of 199.2 nm (3_0^1 band). In all cases, the probe laser center wavelength is 304.5 nm.

5. CONCLUDING REMARKS

This chapter has presented the capabilities of femtosecond velocity map imaging schemes for the detailed description of time-resolved photodissociation dynamics and molecular photodynamics in general. The combination of femtosecond pump-probe tunable laser pulses and a 2D detection technique such as velocity mapping, and the use of selective detection of known quantum states of the product fragments using resonance-enhanced multiphoton ionization has revealed to be an excellent method through the prototype example of the CH_3I molecule, where a broad range of processes can be explored, such as direct dissociation, predissociation, the effect of conical intersections, dimerization, or laser-induced molecular alignment.

Relatively minor experimental changes are required to explore other interesting phenomena with a very similar experimental scheme, like, for instance, Coulomb explosion [55,56]. Also, the possibilities for strong-field control through the introduction of an additional IR ultrashort laser field have been explored with success [57,58]. More and more systems are becoming amenable to be studied by femtosecond velocity map imaging, and there are now examples for small molecules like ammonia [59,60] or larger

molecules like organic chromophores [61-67]. This clearly shows the power of femtosecond velocity map imaging to investigate time-resolved molecular photodynamics.

Acknowledgements

We acknowledge the contributions to the experimental and theoretical work presented in this chapter by J. G. Izquierdo, J. Durá, G. A. Amaral, J. González-Vázquez, G. Gitzinger, M. E. Corrales, G. Balerdi and A. García-Vela. This work has been financed by the Spanish MICINN and MINECO through Grants No. CTQ2008-02578, CTQ2012-37404-C02-01, the Consolider program ‘‘Science and Applications of Ultrafast Ultraintense Lasers’’, Grant No. CSD2007-00013, and by the European Union ITN network ‘‘Ultrafast control of quantum systems by strong laser fields-FASTQUAST’’ (Grant No. PITN-GA-2008-214962). This research has been performed within the Unidad Asociada ‘‘Química Física Molecular’’ between Departamento de Química Física of UCM and CSIC. The facilities provided by the Centro de Láseres Ultrarrápidos (UCM) are gratefully acknowledged.

References

[1] R. Schinke, Photodissociation dynamics, Cambridge University Press, Cambridge, 1993.

[2] M. J. Rosker, M. Dantus and A. H. Zewail, J. Chem. Phys., **89**, 6113 (1988).

[3] A. H. Zewail, Pure App. Chem., **72**, 2219 (2000).

[4] R. de Nalda, J. Durá, J. G. Izquierdo, J. González-Vázquez and L. Bañares, J. Chem. Phys. **128**, 244309 (2008) and references therein.

[5] A. T. J. B. Eppink and D. H. Parker, Rev. Sci. Instrum. **68**, 3477 (1997).

[6] B. J. Whitaker, Image Reconstruction: the Abel Transform, in *Imaging in Chemical Dynamics*, A. G. Suits and R. E. Continetti Eds., American Chemical Society, 2000.

[7] G. A. Garcia, L. Nahon, and I. Powis, Rev. Sci. Instrum. **75**, 4989 (2004).

[8] G. Gitzinger, M. E. Corrales, V. Loriot, R. de Nalda and L. Bañares, J. Chem. Phys. **136**, 074303 (2012).

[9] A. T. J. B. Eppink and D. H. Parker, J. Chem. Phys. **109**, 4758 (1998).

[10] R. N. Zare, Angular Momentum: Understanding Spatial Aspects in Chemistry and Physics (Wiley, New York, 1998); R. N. Dixon, J. Chem. Phys. **85**, 1866 (1986); T. P. Rakitzis and R. N. Zare, J. Chem. Phys. **110**, 3341 (1999).

[11] G. Gitzinger, M. E. Corrales, V. Loriot, G. A. Amaral, R. de Nalda and L. Bañares, J. Chem. Phys. **132**, 234313 (2010).

[12] R. de Nalda, J. Durá, J. González-Vázquez, V. Loriot and L. Bañares, Phys. Chem. Chem. Phys., **13**, 13295 (2011).

[13] D. W. Marquardt, SIAM J. Appl. Math. **11**, 431 (1963); Y. Bard, Nonlinear Parameter Estimation, Academic, New York, 1974; N. R. Draper and H. Smith, Applied Regression Analysis (Wiley Series in Probability and Statistics), Wiley, New York, 1981.

[14] J. González-Vázquez, L. González, I. R. Solá and J. Santamaría, J. Chem. Phys.,**131**, 104302 (2009).

[15] S. Nanbu, T. Ishidab and H. Nakamura, Chem. Sci., **1**, 663 (2010).

[16] B. J. Sussman, D. Townsend, M. Y. Ivanov and A. Stolow, Science, **314**, 278 (2006).

[17] D. R. Yarkony, Rev. Mod. Phys., **68**, 985 (1996).

[18] Y. Amatatsu, S. Yabushita and K. Morokuma, J. Chem. Phys., **104**, 9783 (1996).

[19] A. Gedanken and M. D. Rowe, Chem. Phys. Lett., **34**, 39 (1975).

[20] R. S. Mulliken and E. Teller, Phys. Rev., **61**, 283 (1942).

[21] G. Herzberg, Molecular Spectra and Molecular Structure III. Electronic Spectra and Electronic Structure of Polyatomic molecules, van Nostrand, Princeton, 1996.

[22] R. S. Mulliken, J. Chem. Phys., **8**, 382 (1940).

[23] R. S. Mulliken, Phys. Rev., **50**, 1017 (1936).

[24] F. G. Godwin, C. Paterson and P. A. Gorry, Mol. Phys., **61**, 827 (1987).

[25] Y. Amatatsu, K. Morokuma and S. Yabushita, J. Chem. Phys., **94**, 4858 (1991).

[26] D. Person, P. W. Kash and L. J. Butler, J. Chem. Phys., **94**, 2557 (1991).

[27] J. Durá, G. A. Amaral, R. de Nalda and L. Bañares, J. Chem. Phys., **131**, 134311 (2009).

[28] R. de Nalda, J. G. Izquierdo, J. Durá and L. Bañares, J. Chem. Phys., **126**, 021101 (2007).

[29] H. Guo, J. Chem. Phys., **96**, 6629 (1992).

[30] D. Xie, H. Guo, Y. Amatatsu, and R. Kosloff, J. Phys. Chem. A, **104**, 1009 (2000).

[31] R. O. Loo, G. E. Hall, H.-P. Haerri, and P. L. Houston, J. Phys. Chem., **92**, 5 (1989).

[32] D. W. Chandler, J. W. Thoman Jr., M. H. M. Janssen and D. H. Parker, Chem. Phys. Lett., 156, 151 (1989).

[33] D. W. Chandler, M. H. M. Janssen, S. Stolte, R. N. Strickland, J. W. Thoman, and D. H. Parker, J. Chem. Phys., **94**, 4839 (1990).

[34] A. García-Vela, R. de Nalda, J. Durá, J. González-Vázquez and L. Bañares, J. Chem. Phys., **135**, 154306 (2011).

[35] G. Li, H. J. Hwang, and H. C. Jung, Rev. Sci. Instrum., **76**, 023105 (2005).

[36] M. Dantus, M. J. Rosker, and A. H. Zewail, J. Chem. Phys., **89**, 6128 (1988).

[37] T. S. Rose, M. J. Rosker, and A. H. Zewail, J. Chem. Phys., **91**, 7415 (1989).

[38] J. Durá, R. de Nalda, J. Álvarez, J. G. Izquierdo, G. A. Amaral, and L. Bañares, ChemPhysChem, **9**, 1245 (2008).

[39] J.J. Larsen, H. Sakai, C. P. Safvan, I. Wendt-Larsen, and H. Stapelfeldt, J. Chem. Phys. **111**, 7774 (1999).

[40] B. Friedrich, and D. Herschbach, Phys. Rev. Lett., **74**, 4623 (1995).

[41] T. Seideman, J. Chem. Phys. **115**, 5965 (2001).

[42] F. Rosca-Pruna and M.J.J. Vrakking, J. Chem. Phys., **116**, 6567 (2002).

[43] H. Stapelfeld and T. Seideman, Rev. Mod. Phys., **75**, 543 (2003).

[44] E. Hamilton, T. Seideman, T. Ejdrup, M. D. Poulsen, C. Z. Bisgaard, S. Viftrup and H. Stapelfeld, Phys. Rev. A, **72**, 043402 (2005).

[45] D. E. Folmer, E. S. Wisniewski, S. M. Hurley and A. W. Castleman Jr., Proc. Nat. Acad. Sci. USA, 96, 12980 (1999).

[46] K. V. Vidma, A. V. Baklanov, E. B. Khvorostov, V. N. Ishchenko, S. A. Kochubei, A. T. J. B. Eppink, D. A. Chestakov, and D. H. Parker, J. Chem. Phys. **122**, 204301 (2005).

[47] D. J. Donaldson, V. Vaida, and R. Naaman, J. Chem. Phys. **87**, 2522 (1987).

[48] A. P. Baronavski and J. C. Owrustky, J. Chem. Phys., **108**, 3445 (1998).

[49] S. Felps, P. Hochmann, P. Brint, and S. P. McGlynn, J. Mol. Spectrosc. **59**, 355 (1976).

[50] M. R. Dobber, W. J. Buma, and C. A. de Lange, J. Chem. Phys. **99**, 836 (1993).

[51] S. Eden, P. Limao-Vieira, S. V. Hoffmann, and N. J. Mason, Chem. Phys., **331**, 232 (2007).

[52] V. A. Shubert, M. Rednic, and S. T. Pratt, J. Chem. Phys., **130**, 134306 (2009).

[53] C. Jonah, J. Chem. Phys. **55**, 1915 (1971).

[54] S. Yang and R. Bersohn, J. Chem. Phys. **61**, 4400 (1974).

[55] Y. Wang, S. Zhang, Z. Wei, B. Zhang, J. Phys. Chem. A **112**, 3846 (2008).

[56] M. E. Corrales, G. Gitzinger, J. González-Vázquez, V. Loriot, R. de Nalda, and L. Bañares, J. Phys. Chem. A, **116**, 2669 (2012).

[57] G. Balerdi, M. E. Corrales, G. Gitzinger, J. González-Vázquez, I. R. Solá, V. Loriot, R. de Nalda, and L. Bañares, EPJ Web of Conferences, **41**, 02035 (2013).

[58] M. E. Corrales, G. Balerdi, V. Loriot, R. de Nalda, and L. Bañares, Faraday Discuss. (2013). DOI: 10.1039/c2fd20143g.

[59] K. L. Wells, G. Perriam, and V. G. Stavros, J. Chem. Phys. **130**, 074308 (2009).

[60] N. L. Evans, H. Yu, G. M. Roberts, V. G. Stavros, and S. Ullrich, Phys. Chem. Chem. Phys., **14**, 10401 (2012).

[61] A. Iqbal, M. S. Y. Cheung, M. G. D. Nix, and V. G. Stavros, J. Phys. Chem. A, **113**, 8157 (2009).

[62] A. Iqbal, and V. G. Stavros, J. Phys. Chem. A, **114**, 68 (2010).

[63] K. L. Wells, D. J. Hadden, M. G. D. Nix, and V. G. Stavros, J. Phys. Chem. Lett., **1**, 993 (2010).

[64] D. J. Hadden, C. A. Williams, G. M. Roberts, and V. G. Stavros, Phys. Chem. Chem. Phys., **13**, 4494 (2011).

[65] G. M. Roberts, A. S. Chatterley, J. D. Young, and V. G. Stavros, J. Phys. Chem. Lett., 3, 348 (2012).

[66] G. M. Roberts, C. A. Williams, J. D. Young, S. Ullrich, M. J. Paterson, and V. G. Stavros, J. Am. Chem. Soc., **134**, 12578 (2012).

[67] G. M. Roberts, C. A. Williams, H. Yu, A. S. Chatterley, J. D. Young, S. Ullrich, and V. G. Stavros, (2013) DOI: 10.1039/cf2d20140b.